IOP Publishing Measurement Science and Technology
Journal **XX** (XXXX) XXXXXX https://doi.org/XXXX/XXXX

A Polynomial Model with Line-of-Sight Constraints for Lagrangian Particle Tracking Under Interface Refraction

Xin Zeng[1,2], Hao Qu[1,2], Chuangxin He[1,2,*], Yingzheng Liu[1,2], and Lian Gan[3]

[1]Key Laboratory of Education Ministry for Power Machinery and Engineering/School of Mechanical Engineering, Shanghai Jiao Tong University, Shanghai, People's Republic of China
[2] Gas Turbine Research Institute/School of Mechanical Engineering, Shanghai Jiaotong University, Shanghai, People's Republic of China
[3]Department of Engineering, Durham University, Durham, UK

E-mail: chuangxin.he@sjtu.edu.cn (C. He)

Received xxxxxx
Accepted for publication xxxxxx
Published xxxxxx

Abstract

This paper introduces an improvement of the "Shake-The-Box (STB)" (Schanz, Gesemann, and Schröder, Exp. Fluids 57.5, 2016) technique using the polynomial calibration model and the line-of-sight constraints (LOSC) to overcome the refractive interface issues in Lagrangian particle tracking (LPT) measurement. The method (named LOSC-LPT) draws inspiration from the two-plane polynomial camera calibration in tomographic particle image velocimetry (Tomo-PIV) (Worth and Nickels, Thesis, 2010) and the STB-based open-source Lagrangian particle tracking (OpenLPT) framework (Tan, Salibindla, Masuk, and Ni, Exp. Fluids 61.2, 2019). The LOSC-LPT introduces polynomial mapping functions into STB calibration in conditions involving gas–solid–liquid interfaces at container walls exhibiting large refractive index variations, which facilitates the realization of particle stereo matching, three-dimensional (3D) triangulation, iterative particle reconstruction, and further refinement of 3D particle position by shaking the LOS. Performance evaluation based on synthetic noise-free images with a particle image density of 0.05 particle per pixel (ppp) in the presence of refractive interfaces demonstrates that LOSC-LPT can detect a higher number of particles and exhibits lower position uncertainty in the reconstructed particles, resulting in higher accuracy and robustness than that achieved with OpenLPT. In the application to an elliptical jet flow in an octagonal tank with refractive interfaces, the use of polynomial mapping results in smaller errors (mean calibration error < 0.1 px) and thus more long trajectories identified by LOSC-LPT (13,000) compared with OpenLPT (4,500) which uses the pinhole Tsai model (mean calibration error > 1.0 px). Moreover, 3D flow-field reconstructions demonstrate that the LOSC-LPT framework can recover a more accurate 3D Eulerian flow field and capture more complete coherent structures in the flow, and thus holds great potential for widespread application in 3D experimental fluid measurements.

Keywords: Lagrangian particle tracking, camera calibration, polynomial camera model, refractive interface

1. Introduction

Advanced four-dimensional Lagrangian particle tracking velocimetry (LPT) methods, represented by the "shake-the-box" (STB) technique [1, 2], enable much higher spatial resolution flow measurements than tomographic particle image velocimetry (Tomo-PIV) [3], avoiding the spatial filtering effect arising from cross-correlation analysis in Tomo-PIV and minimizes the occurrence of ghost particles. STB requires precise and efficient camera calibration, such as the pinhole camera model [4], for repeated particle reprojection during the iterative particle reconstruction (IPR) procedure [5] and particle correction. However, when refractive interfaces exist between the cameras and the measurement target, which are commonly encountered in experiments in water [6], the efficient pinhole model yields significant calibration error even with a small angle between the camera optical axis and interface normal. In this context, polynomial mapping functions are more flexible alternatives that can capture nonlinearities in the imaging system [6] and have been widely applied in Tomo-PIV [7, 8]. However, repeated projection of the 3D particle positions in the fluid domain onto camera images using polynomials is quite challenging and imprecise, causing large errors in the interpolation of the particle positions during the projection and correction steps. Much effort should be made on the precise and efficient polynomial mapping procedure for the STB method applied for interface refraction.

The LPT method [9] is derived from classical particle tracking velocimetry (PTV) and enables the three-dimensional (3D) reconstruction and tracking of long particle trajectories based on triangulation and track linking. The development of the STB technique [1] transforms the processes of triangulation-then-tracking [10] in classical 3D-PTV into tracking-prediction-triangulation. This approach involves the use of the existing tracks to predict the particle location in the next time-step, followed by the implementation of IPR with the predicted location reprojection using a camera model. This enables the measurement of flow fields with much higher resolution than that can be achieved by Tomo-PIV under high particle density [11, 12]. Notably, the STB algorithm in LPT is quite flexible and can be combined with any calibration models, however, the successful application of STB relies on accurate camera calibration, with a typical requirement of a calibration error lower than 0.1 px. Pinhole camera models [1, 13] are commonly used as they are efficient for the repeated reprojection of 3D particle positions onto images. Indeed, the pinhole models perform well with the assumption that the LOSs between the particles in the fluid domain and the camera center are straight. However, several scenarios are commonly encountered in experiments in water where the refractive interfaces exist. This deflects the LOSs at the interfaces and usually results in a calibration error larger than 2 px when using the pinhole model for camera calibration. This calibration error cannot be reduced by volume self-calibration (VSC) [14, 15], in which only the parameters of the pinhole model are updated while the refraction effects on the model form are still not considered. Recently, an extended IPR with "global shake" approach by Jahn et al. [16] has shown great potential to solve problems IPR for high particle concentration, and correction for both initial decalibrations of camera calibration. However, numerous studies focus on the improvement of pinhole camera model with refractive interface effects. The bundle adjustment approaches using ray tracing [17-21] can accurately correct each deviated line of sight (LOS) between the particles and camera center in the presence of a refractive interface. These approaches use ray tracing based on Snell's law and the co-planarity of the surface normal vector with the incident and refracted rays, which requires many loops of iteration for each LOS. It is extraordinarily time-consuming and is rarely applied in 3D-PTV or LPT measurement where millions of LOSs need to be determined. Several novel pinhole camera models [22, 23] have been introduced to overcome the challenges associated with refractive index variations. Paolillo and Astarita [23] developed a ray-tracing camera model for the measurements inside a transparent cylinder immersed in water. This model has an accuracy equivalent to the case of a 7^{th}-order polynomial model discussion in Paolillo and Astarita [6], but still requires time-consuming iterations. Acher et al. [22] presented a new camera model based on the combination of an analytical model (e.g. linear or polynomial) and a local discrete correction, saving all the corrections to the projection and back-projection functions in two adaptive grids and refining the grid locally enough to meet the required accuracy. The local discrete correction is similar to the work by Schanz et al. [24], the "2D-shaking" method that varies the peak location on a single camera to minimize the local residuum, which applied to correct the projected positions of particles seen by a certain camera to best fit the original camera image, a "2D correction maps" is built, which is obtained by averaging disparities between the reprojection 2D positions on the different cameras and particle peak present at the source image, the "2D correction maps" can be used to correct a location projected from 3D space to a 2D camera image, with a simply shift according to the deflection value at this position given by the average calibrated map. However, the local discrete correction or "2D correction maps" may need a good initialization, which means that the corrections are performed based on an accurate enough camera model such as a pinhole model or a polynomial model, meanwhile under a high calibration error, it may need many time-consuming grid searching, interpolation calculations, and grid refinement. All the above-mentioned strategies try to improve the pinhole model with refractive correction at the expense of efficiency. Such

methods yield several orders of computational time increasing when implemented in 3D-PTV or LPT and thus may not be the best choice for the STB with frequent projection and 3D reconstruction.

The polynomial camera model can capture nonlinearities in the imaging system through higher-order terms, represented as polynomials, multi-plane polynomials, and rational functions with different orders. Typically, for polynomials or rational functions, 7^{th} orders ($7 \times 7 \times 7$) at each dimension of world coordinates (X, Y, Z) is required to ensure small errors according to Paolillo and Astarita [6]. This involves a large number of parameters and results in complexities in the key particle reprojection in the triangulation and IPR procedures. Barta et al. [25] used the Soloff mapping functions [26] with 16 parameters of the 3^{rd} order ($3 \times 3 \times 3$) models for triangulation. However, an iterative process was required to determine the LOS by two points as well as the partial derivatives of the mapping functions [27]. This required multiple Z-position planes to obtain sufficiently accurate 3D mapping functions, and the recovery of the 3D particle positions was cumbersome due to the excessive number of iterations. We have noted that the multi-plane polynomials that the calibration parameters are the polynomial coefficients only for X, Y coordinates in each Z_i-plane, then simple linearly interpolating 3D particle positions along the Z-direction to obtain the image coordinates (Z-interpolation), showing similar performance compared with the best rational models with 7^{th}-order [6], but have much simpler calibration procedure and the reduced number of parameters. This multi-plane polynomial camera model [26] has been applied in 3D tomographic reconstruction of Tomo-PIV [7, 8] to enhance accuracy, assuming that the LOSs between two planes are linear, its mapping functions between points on calibration planes and images can be accurately represented using only 10 parameters in a 3^{rd}-order model. In addition, the determination of LOSs between two planes for the 3D position reconstruction can be found in works [28, 29], while the projection of the 3D particle positions onto camera images using multi-plane polynomials model is not easy and challenging, a common projection idea is to find the point where the LOS intersects the image plane, which is difficult to achieve in the presence of refractive interfaces. The projection of particles onto the images by Z-interpolation according to particle position between multi Z-plane might be non-physical due to the LOSs of pixels is not parallel [6], causing reprojection error of several pixels (px) and huge triangulation error for PTV (will be discussed in Section 2.3 in details). Therefore, LOS interpolation must be implemented to achieve the sub-pixel accuracy of the projected particle images [6], which is based on the assumption that straight LOSs in the fluid and each LOS through a pixel can be determined by two points on two calibration planes. When refractive interfaces exist and meanwhile the angle (φ_1) between the camera optical axis and interface normal is large, the reprojection onto images by linear LOS interpolation causing a reprojection error of approximately 0.2 px and a triangulation error of the same level during the particle shaking step with LOS interpolation reprojection (will be discussed in Section 2.3). Thus, a strategy of LOS constraints is designed and implemented to solve this error accumulation. After shaking the 3D particle positions with interpolation projection, the 2D particle centers on the image are also corrected by "2D-shaking", resulting in a new LOS with two calibration planes, which is similar to the ray of light (LOS) moving with the displacement of its light source (2D particle center). The latter is named LOS constraints (LOSC) in our present implement.

Considering these aspects, the objective of this study is to provide an improvement of the "Shake-The-Box (STB)" of LPT using the polynomial calibration model in Tomo-PIV. The method (named LOSC-LPT) introduces polynomial mapping functions into STB calibration, camera calibration is performed using only two planes and expressed using polynomial functions. An effective LOS interpolation approach using polynomial functions is designed and applied to ensure accurate reprojection during stereo matching, 3D particle reconstruction, IPR, and shaking process of STB in conditions involving gas–solid–liquid interfaces at container walls exhibiting large refractive index variations. A precise and efficient way based on LOS interpolation and LOS constraints by shaking the LOSs based on two-plane polynomial calibration is added to realize the refinement of 3D particle positions after IPR and STB. The accuracy, convergence, and robustness are evaluated using synthetic particle images from the Johns Hopkins turbulence database (JHTDB) [30]. Additionally, the proposed framework is applied to an experimental study of a jet from an elliptical nozzle with an aspect ratio (AR) of 2, to capture the vortex dynamics of the elliptical jet.

2. Methodology

The LOSC-LPT framework is realized based on introducing camera calibration with two planes [7, 8] into the STB of LPT, the particle tracking process is inspired by the shake-the-box (STB) [1] technique and the open-source Lagrangian particle tracking (OpenLPT) framework [13, 31]. This section describes the camera calibration of two-plane polynomial mapping functions, and its application for the particle reprojection onto the image, and the LOS constraint procedure for refinement of particle 3D position.

2.1 Camera calibration

Camera calibration is to establish mapping functions from 3D space to the 2D image for the camera, the process can be represented [4, 32], pinhole camera calibration can be performed using the Tsai two-step calibration [4] or Zhang Zhengyou calibration [32] methods by optimizing the abovementioned camera parameters and quantifying any image distortions during recording. The pinhole model is highly accurate when the world position and camera are in the same medium, with mean calibration errors smaller than 1e-5 px, as shown in Fig. 1b, all calibration errors are assessed using synthetic images generated by the modified alternating forward ray tracing (AFRT) method by Mulsow [17] and Belden [18]. However, PIV measurements typically involve cameras that capture images in air through a transparent tank or container (made of glass or acrylic) containing water or another fluid. In this condition, the pinhole model between the world and image points fails because the pinhole model assumes that the LOSs are straight lines and neglects the refraction of light. As shown in Fig. 1a, the 2D particle centers (green points) in the image without interfaces are considerably different from those (blue points) in the case with refractive interfaces. Even when the world (P_i' and P_i") and image points (P_i) (in blue points) are exactly known in the synthetic dataset, the LOSs from all 3D world points do not meet in a single point (camera center) during the pinhole camera model calibration, and then the resulting pinhole model exhibits substantial errors (Fig. 1c), and the point positions on the image deviate from those obtained through the direct application of the pinhole Tsai camera model under considering only radial distortion, with a maximal calibration error exceeding 2.0 px, as discussed by Treibitz et al. [33].

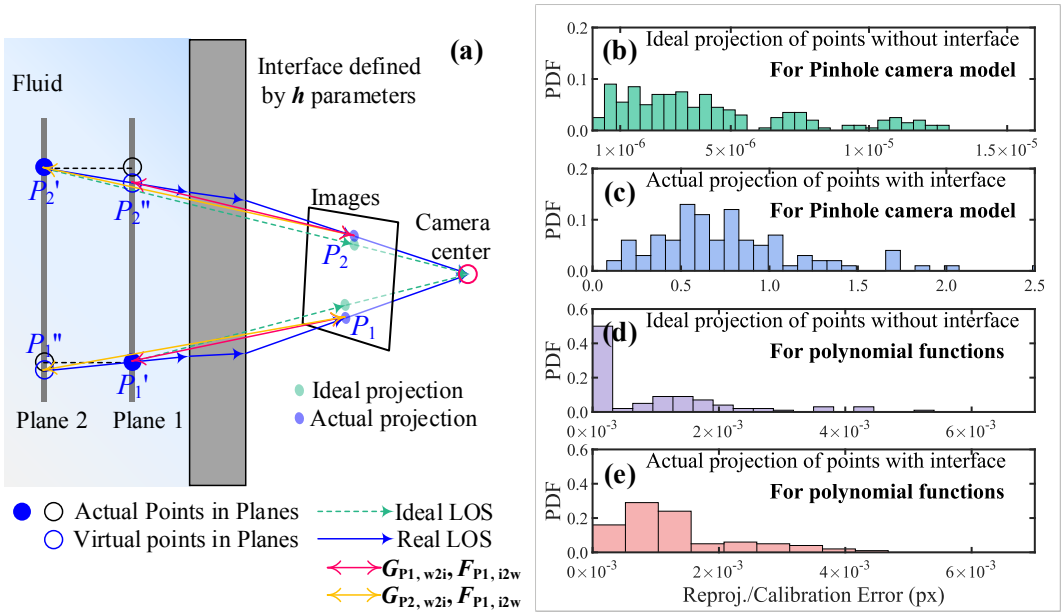

Figure 1 (a) Schematic of imaging through refractive interfaces. The projected point position (blue line and projection) on the image with refractive interfaces deviates from that (green dash line and projection) obtained by directly applying the pinhole Tsai camera model. As well as the schematic of lines-of-sight (LOS, green dash lines or blue lines) based on calibration by two planes are shown, using a third-order polynomial for 2D points P_i (u, v) in images corresponding to the 3D physical world coordinates P_i' ($\boldsymbol{F}_{\mathrm{P1,\,w2i}}$, $\boldsymbol{G}_{\mathrm{P1,\,i2w}}$) or P_i" ($\boldsymbol{F}_{\mathrm{P2,\,w2i}}$, $\boldsymbol{G}_{\mathrm{P2,\,i2w}}$) in each Z-plane. Comparison of reprojection or calibration errors using the pinhole Tsai model in scenarios without (b), or with refractive interfaces (c). Comparison of reprojection or calibration errors from using the third-order polynomial in scenarios without (d), or with refractive interfaces (e). All calibration errors are assessed using synthetic images generated by the modified alternating forward ray tracing (AFRT) method.

In this context, polynomial mapping functions are more flexible and can capture the nonlinearities in an imaging system through higher-order terms [6]. The mapping functions from the 3D space to the 2D image for the camera can be represented as polynomials or two-plane polynomials with different orders. For the two-plane polynomial model in the z-direction can be simplified as the calibration for polynomial the mapping functions $\boldsymbol{G}_{\mathrm{p,\,w2i}}$ from each 2D Z-plane to the 2D image for the camera are polynomials:

$$u = a_0 + a_1X + a_2X^2 + a_3X^3 + a_4Y + a_5Y^2 + a_6Y^3 + a_7XY + a_8X^2Y + a_9XY^2 \quad , \tag{1}$$

$$v = b_0 + b_1X + b_2X^2 + b_3X^3 + b_4Y + b_5Y^2 + b_6Y^3 + b_7XY + b_8X^2Y + b_9XY^2 , \quad (2)$$

where, u and v are the 2D pixel coordinates on the image in two directions, respectively; (a_i, b_i) are the coefficients of the polynomial model in the kth Z-plane for , X, Y are point positions in calibration plane in world coordinate system. Similarly, the mapping functions $\boldsymbol{F}_{\mathbf{p,\ i2w}}$ from the 2D image in u and v to the 2D plane in X and Y for the camera are expressed with the 3th-order polynomials for the triangulation:

$$X = c_0 + c_1u + c_2u^2 + c_3u^3 + c_4v + c_5v^2 + c_6v^3 + c_7uv + c_8u^2v + c_9uv^2 , \quad (3)$$

$$Y = d_0 + d_1u + d_2u^2 + d_3u^3 + d_4v + d_5v^2 + d_6v^3 + d_7uv + d_8u^2v + d_9uv^2 . \quad (4)$$

The calibration coefficients a_i, b_i, c_i, and d_i of each plane are fitted using the least square method with the 2D image pixel coordinate points in u and v and the exact world coordinate 3D points in the 2D plane in X and Y. The 3-order polynomials are selected in this work with 40 parameters for each plane to image, and the number of orders can be raised for a better calibration accuracy in more complex scenarios.

It is worth noting that only the polynomial mapping function from each 2D Z-plane to the 2D image is calibrated, as shown in Fig. 1a, the $\boldsymbol{F}_{\mathbf{P1,\ i2w}}$ (Orange line arrow arrow) and $\boldsymbol{F}_{\mathbf{P2,\ i2w}}$ (Red line arrow) are mapping function for image point (P_i) to Plane1 point (P_i') and Plane2 point (P_i''), the inverse polynomial functions $\boldsymbol{G}_{\mathbf{P1,\ w2i}}$ and $\boldsymbol{G}_{\mathbf{P2,\ w2i}}$ are respectively mapping function for Plane1 point (P_i') to image point (P_i) and Plane2 point (P_i'') to image point (P_i), respectively. If the image point (P_i) is known, next the Plane1 point (P_i') and Plane2 point (P_i'') can be calculated by $\boldsymbol{F}_{\mathbf{P1,\ i2w}}$ and $\boldsymbol{F}_{\mathbf{P2,\ i2w}}$, then a LOS ($P_i$'$\rightarrow$ P_i'') can be determined. This strategy is built on each LOS remains straight in the fluid, which is accepted in almost all Tomo-PIV because the tomographic reconstruction of voxels relies on the voxels crossed by straight LOS [7]. Note that the calibration coefficients a_i, b_i, c_i, and d_i are accurate only in the target Z-position, and Z-interpolation is usually applied for the reprojection at other Z-positions, which may be non-physical and imprecise when the angle between the camera optical axis and interface normal is large, therefore the reprojection algorithm are realized based on LOS interpolation in this work. By above strategy, the refractive interface can be neglected and the effect of light refraction is removed, and the camera center in pinhole camera model is not necessary. Note that the P_1' and P_2' need not be the fixed calibration points in checkerboard calibration plate, they can be any points in calibration plane (fixed Z), and each LOS can be recovered if we know any one of P_i', P_i'' and 2D center P_i in image. The presence of refractive interfaces does not considerably affect the calibration, as shown in Fig. 1e-f, as the mean calibration errors in cases with and without refractive interfaces are lower than 1e-3 px.

In this work, the polynomial mapping functions are calibrated with two positions in depth throughout the volume; reprojection for stereo matching, triangulation, IPR, and shaking of STB are redesigned; and a novel shaking the LOS strategy named LOS constraints (LOSC) is developed to refine 3D particle positions based on two-planes polynomial camera calibration. The stereo matching, triangulation, and shaking for IPR are important parts of IPR [5], the stereo-matching algorithm [9] with the camera model is a combination of the algorithms proposed by Dracos [34] and Mann and Ott [35]. Stereo matching is accomplished through epipolar line reprojection, in which the LOS of camera 1 through the illuminated volume from Z1 to Z2 is projected onto the image of camera 2, thereby capturing the nearest neighbor matching 2D particle center near the epipolar line reprojection with an uncertainty range of $\pm\varepsilon_{\max}$. Subsequently, the 3D particle position (X, Y, Z) is reconstructed by triangulation of each combination of 2D particle centers in the images of cameras 1 and 2. To confirm the accuracy of the reconstructed particles, the presence of each 3D particle is verified in the images of camera 3 and 4 within $\pm\varepsilon_{\max}$ around the projection of the 3D particle position (X, Y, Z) onto these images. The uncertainty in stereo matching and triangulation is typically set according to the calibration error. Shaking is repeatedly conducted during the IPR and after prediction to refine the 3D particle positions [1, 5, 13]. Then the detected particles and their projection on each camera image are removed and a new round of IPR is performed using the residual image. For the scenarios with refractive interfaces, the LOSs deflect at the interface, and their direction vectors in the fluids cannot be precisely and promptly located using the pinhole camera model. The LOSs can be determined with intersections of LOSs in two planes using the polynomial mapping functions, then the stereo matching can be executed successfully. Then each 3D particle position coordinates are then computed using a least squares solution of the LOSs from all camera images.

2.2 Reprojection by LOS interpolation

Following stereo matching and triangulation in the IPR [5], the shaking process is applied to refine the 3D particle positions, which is also a key process after prediction using the Wiener filter in the STB. Shaking is performed in a small 3D space by

projecting the particles onto all camera images using the OTF parameters. The objective is to determine the least difference (summing $I_{res.}$ over all pixels of local residual images) between the reprojection image and original particle image, enabling the reconstruction of more particles from the residual images by IPR. Notably, the reprojection of 3D particle positions onto the images is a critical and frequent step. Any 3D particle position can be projected onto the image using the camera model from pinhole Tsai model in a straightforward manner. However, projecting 3D particle positions outside the calibration planes onto images based on the two-plane polynomial mapping functions from Eqs. (1-2) is challenging. As shown in Fig.2a, the projection coordinates [u, v] on the image are typically obtained by evaluating the polynomial functions in Eqs. (1-2) of the world 3D position P_p [X_p, Y_p, Z_p] on the Z_p-planes with $Z = Z_k$ using [X_p, Y_p], obtaining the projection coordinates [u', v'] of P_1' and [u", v"] of P_1", subsequently, the projection coordinates [u, v] are linearly interpolated along the Z-direction according to the position of P_p between P_1' to P_1" from Fig. 2b. Z-interpolation may be non-physical and imprecise when the angle between the camera optical axis and interface normal is large, the maximal reprojection error of particles with refractive interface are over 1.0 px in Fig.2e. To enhance the accuracy, LOS interpolation must be implemented [6]. Thus, in this study, LOS interpolation is applied to ensure accurate reprojection.

As shown in Fig.2c, the reprojection algorithm based on LOS interpolation involves the following steps: First, all the LOSs of image pixels for each camera are computed based on the two-plane polynomial functions in Eqs. (1-2) with two calibration planes, each 2D center P_i can determine two points P_i' and P_i" in two planes from Fig. 1 or Fig.2, then a LOS can be determined with the two points P_i' and P_i", and then temporarily stored in a lookup table. Each LOS consists of four elements, i.e., (1) image pixel coordinates [u, v] of all the pixel points in each camera image, (2) points P_i' in world coordinates on the intersections of LOS across the first calibration plane, (3) points P_i" in world coordinates on the intersections of LOS across the second calibration plane, and (4) the normalized unit vector of the LOS. Second, for a 3D particle world coordinate P_p [X_p, Y_p, Z_p] obtained by triangulation in IPR or prediction using the Wiener filter in STB, all the intersections [X_{LOS}, Y_{LOS}, Z_p] of the LOSs of all pixels across the virtual Z_p-plane are calculated, and their Euclidean distance to the coordinate P_p [X_p, Y_p, Z_p] is stored. An intersection [X_{LOS}, Y_{LOS}, Z_p] of the LOS with the least Euclidean distance to the coordinate [X_p, Y_p, Z_p] (red circle) is searched and recorded, as indicated by the purple circle in Fig.2d, and this intersection corresponds to a LOS in the lookup table. Note that the calculation and searching procedure for intersections of this particle can be terminated once the intersection with the least Euclidean distance has been recorded. Third, based on Fig.2d, sub-pixel coordinates [u_p, v_p] can be interpolated in the four pixels corresponding to the four LOSs (as green, orange, light blue and purple dashed lines) around the intersection with coordinates [X_{LOS}, Y_{LOS}, Z_p] in red circle. As displayed in Fig.2f, the reprojection errors are evaluated using synthetic particle images, revealing that mean reprojection errors of particles by LOS interpolation are less than 0.10 px, which is much smaller than those by Z-interpolation. Note that the maximum reprojection errors of particles are over 0.1 px from Fig.2f, therefore a new strategy named LOS constraints (LOSC) is introduced for reducing the particles 3D reconstruction error.

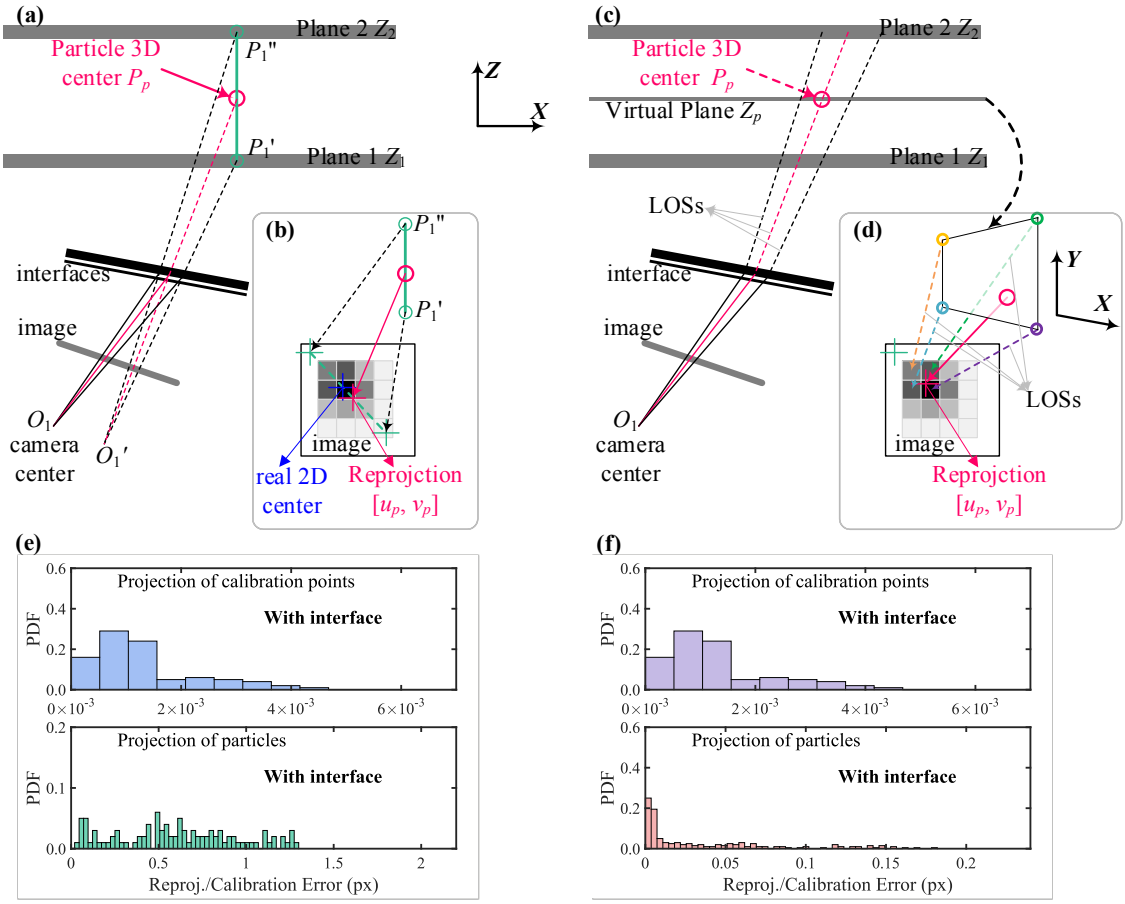

Figure 2 (a)(b) Schematic of particle reprojection by *Z*-interpolation with two calibration planes. (c)(d) Schematic of particle reprojection by LOS interpolation with two calibration planes. (e) Reprojection or calibration errors of calibration points or particles from *Z*-interpolation with refractive interface. (f) Reprojection or calibration errors of calibration points or particles from LOS interpolation with refractive interface.

2.3 LOS constraints

The shaking of the 3D particle position is frequently performed after stereo matching and 3D triangulation in the IPR [13] and after the Wiener filter prediction in the STB [1]. Figure 3 schematically illustrates the repeated shaking in the STB process. The 3D particle coordinate is adjusted in all three dimensions [$\pm\Delta X$, $\pm\Delta Y$, $\pm\Delta Z$] by projecting its coordinate onto the image and recording the residual difference (summing $I_{res.}$ over all pixels of the local residual images) between the reprojection image and original particle image. For example, in the *X*-dimension, the residual values at -ΔX, 0, +ΔX are recorded and fitted to a quadratic polynomial function in Fig. 3d, and then the minimal value is solved using the quadratic polynomial function, which corresponds to the optimal 3D particle world coordinates. This process is also repeated for the *Y*- and *Z*-dimensions [5]. Shaking is an iterative process, and the initial shaking 3D range can be based on the calibration error or particle acceleration. Subsequent shaking widths are half of the width in the last iteration, and the process is typically terminated after a specific number of iterations. When there are no refractive interfaces, the 3D particle coordinate can be accurately reconstructed by 3D triangulation using all 2D particle centers after shaking on the images of several cameras and the camera model from Fig. 3. However, when refractive interfaces exist, the shaking process with the camera model requires a larger initial shaking 3D width or more iterations, and moreover, the LOSs do not usually meet at a single point in the 3D triangulation. When the polynomial mapping functions are used, the calibration error is small, thus the initial shaking 3D width and the number of iterations will be small. The initial shaking 3D width or number of iterations is nearly the same in the cases with and without refractive interfaces thanks to the mean calibration errors in cases with and without refractive interfaces are lower than 1e-3 px from Fig.1d-e. Additionally, the shaking process is slightly different than that with the camera model. The shaking of particle *Z*-position is first performed to determine the virtual *Z*-plane from Fig. 3c for reprojection based on interpolation, followed by shaking the particle *X* and *Y* positions using LOS interpolation.

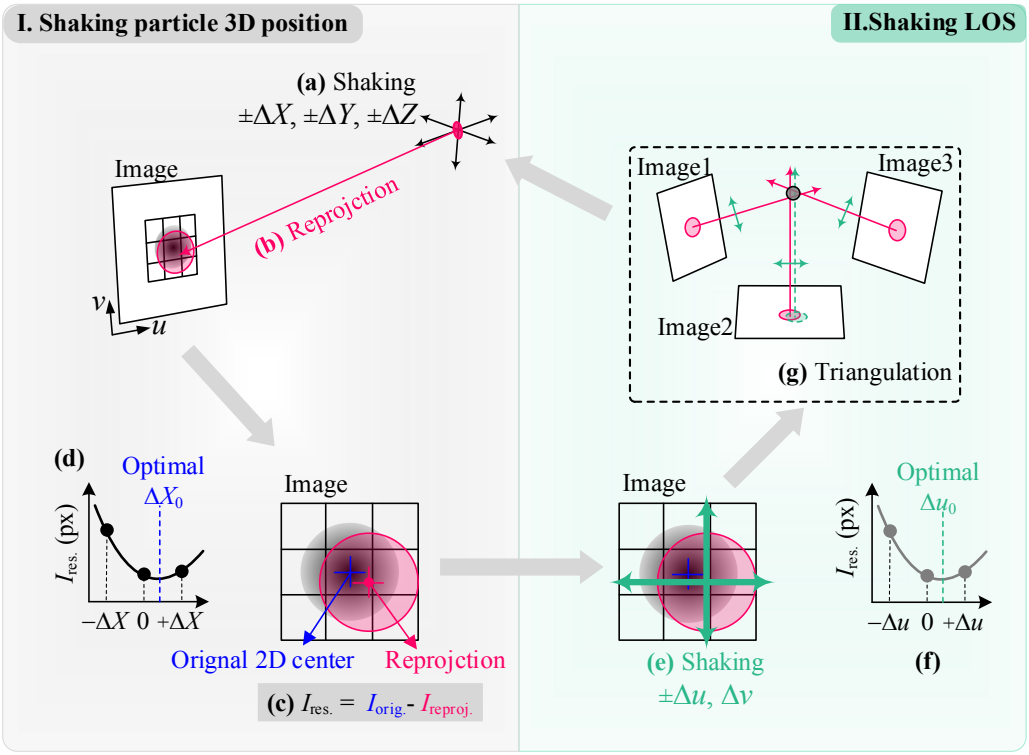

Figure 3 Schematic of the line-of-sight constraints (LOSC) in LOSC-LPT, based on STB algorithm.

Despite repeated shaking, the particle position reconstructed by 3D triangulation with all the 2D particle centers still involves certain errors, caused by the LOS interpolation from Fig. 2f, due to four neighboring LOS points that are not regular distribution in the virtual plane. The linear LOS interpolation is selected for higher efficiency, while the nonlinearity in imaging cannot be interpolated linearly. Thus, the minimal value determined from the quadratic polynomial function during shaking exhibits significant errors, and cause that the least square solution (triangulation point) of the LOSs from all cameras are slightly different from the particle position. To solve this problem, a new strategy named LOS constraints (LOSC) is introduced: After shaking the 3D particle position with interpolation projection, the 2D particle center on the image with OTF parameters is corrected yielding the least difference (summing $I_{res.}$ over all pixels of local residual images) between the new particle image and the original one, as shown in Fig. 3c. Subsequently, the LOSs are shaken with respect to the 2D particle centers as shown in Fig. 3e, while the directions of the LOSs remain unchanged; this is similar to a ray of light moving with the movement of its light source. The summing $I_{res.}$ over all pixels of local residual images at $-\Delta u$, 0, $+\Delta u$ for the u-direction in the image, $-\Delta v$, 0, $+\Delta v$ for the v-direction in the image are recorded and fitted to a quadratic polynomial function during the shaking process in Fig. 3f, and the minimal value is then solved from the quadratic polynomial function, representing the optimal reprojection of 3D particle world coordinates. This process is similar to the "2D-shaking" by Schanz et al. [24] that varies the peak location on a single camera to minimize the local residuum, which applied to correct the projected positions of particles seen by a certain camera to best fit the original camera image. Then from the optimal reprojection position, the LOSs can be determined with intersections of LOSs in two planes using the polynomial mapping functions, and then the exact 3D particle position can be triangulation reconstruction with a least squares solution of the LOSs from all camera images [35]. Although LOS interpolation has some errors, the intersections of LOSs in two calibration planes using the polynomial mapping functions are very precise, and the LOSs where the particle is located at can be accurately reconstructed. This procedure can effectively reduce the 3D reconstruction error to less than 0.1px, with the fact that the triangulation of the 3D particles based on the calibrated polynomial function (Eqs. (1-2)) is precise while the interpolation error in the 3D-to-2D projection can be corrected. The initial shaking 2D width can be set as the final shaking 3D width by converting physical coordinates to pixel coordinates, and the number of iterations can be made consistent in both cases.

By combining the abovementioned strategies of polynomial function calibration, reprojection based on LOS interpolation, 3D shaking, and LOSC, we realize an LPT framework as LOSC-LPT based on the original STB, and then the performance

evaluation is conducted using synthetic images and an experimental dataset in the presence of refractive interfaces. The determination of LOSs between two planes for the 3D position reconstruction is referred to the works [28, 29], and the stereo matching with two planes and LOS constraints are built upon the particle triangulation procedure by Dracos [34] and Mann and Ott [35], the track linking and STB parts of particle tracking are based on the methods proposed by Ouellette et al. [9], Schanz et al. [1], and Tan et al. [13], and track initialization is based on IPR [5] and 4BE-ETI [36], or particle–space correlation [37]. This framework has been parallelized based on open multi-processing (OpenMP) with the CPU [38] and will be further improved using the compute unified device architecture (CUDA) [39] with graphics processing unit (GPU) devices in the future.

3. Synthetic data validation

3.1 Synthetic 3D experimental setup

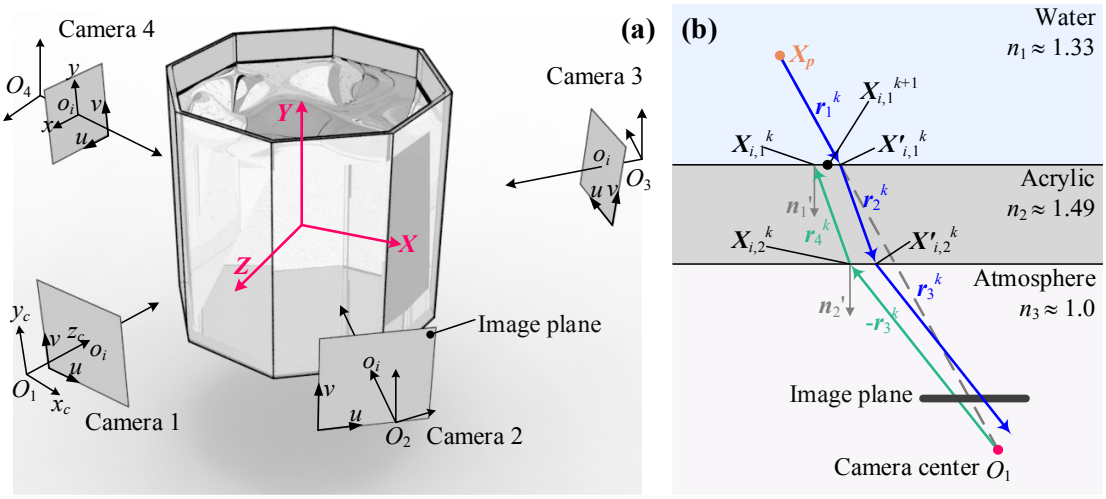

Figure 4 (a) Definitions of world, camera, and image coordinate systems for a multi-camera setup with refractive interfaces. Octagonal water tank. The distance D_{octagon} between the inner wall of the tank and world origin (0, 0, 0) is 200 mm, and the thickness h_{octagon} of the water tank is 20 mm. (b) Schematic of the alternating forward ray tracing (AFRT) procedure for synthetic particle images.

The accuracy, convergence, and robustness of the LOSC-LPT framework are evaluated using a synthetic image dataset generated from a synthetic 3D experimental setup simulating particle motion in an isotropic-turbulence flow from the JHTDB [30]. In the absence of refractive interfaces, synthetic images can be easily generated using the pinhole camera model. However, the complexity of image generation increases in the presence of refractive interfaces. To address this problem, a synthetic particle image code with refractive interfaces based on the modified alternating forward ray tracing (AFRT) method is realized, building upon the methods of Mulsow [17] and Belden [18]. The modified AFRT algorithm can effectively produce highly accurate datasets closely resembling real experimental data with interfaces. Figure 4b illustrates the AFRT procedure in the octagonal water tanks, along with the definitions of the world, camera, and image coordinate systems, for synthetic images in the multi-camera setup with refractive interfaces. The details of the synthetic particle image procedure AFRT are only briefly described herein, and details can be found in the work of Belden [18]. From Fig. 4a, *X*-*Y*-*Z* is the fixed world coordinate system, which can be positioned arbitrarily. x_c-y_c-z_c is the camera coordinate system, with its origin located at the camera center O_c. The physical and pixel coordinates at the image plane are *x*-*y* and *u*-*v*, respectively. For an octagonal water tank, the distance D_{octagon} between the inner wall of the tank and world origin [0, 0, 0] is 200 mm, and the thickness parameter h_{octagon} of the water tank is 20 mm (Fig. 4a). The centers of the four cameras are summarized in Table 1. All cameras have a focal length of 120 mm. The centers of the image planes are also computed and presented in Table 1, the camera setup is designed with the cameras rotated 5° along the x_c axis of the camera coordinate system to simulate installation error. The layout of the four cameras from the top view of the tank is shown in Fig. 8a.

Table 1 Definitions of the world, camera, and image coordinate systems

Camera ID	Focal length f (mm)	x_c-axis θ (°)	y_c-axis φ (°)	z_c-axis ω (°)	Center of camera O_c (mm)	Center of image plane O_i (mm)
1	120	5	0	0	400·[-sin(π/8),0,-cos(π/8)]	280·[-sin(π/8),0,-cos(π/8)]
2	120	5	0	0	400·[sin(π/8),0,-cos(π/8)]	280·[sin(π/8),0,-cos(π/8)]
3	120	5	0	0	400·[cos(π/8),0,sin(π/8)]	280·[cos(π/8),0,sin(π/8)]
4	120	5	0	0	400·[-cos(π/8),0,sin(π/8)]	280·[-cos(π/8),0,sin(π/8)]

The Gaussian intensity profile is used for each particle distribution in synthetic images, with the OTF parameters [5] covering various experimental optical distortion effects such as blurring and astigmatism:

$$I^i_{\text{part}}(x_i, y_i, p) = ae^{-(bx'^2+cy'^2)}, \tag{5}$$

along with rotation effects:

$$x' = (x_i - x_{ip})\cos\alpha + (y_i - y_{ip})\sin\alpha, \tag{6}$$

$$y' = -(x_i - x_{ip})\sin\alpha + (y_i - y_{ip})\cos\alpha, \tag{7}$$

where $[x_{ip}, y_{ip}]$ is the particle image center, that is, the intersection of the LOS and image plane in pixel units; and $[x_i, y_i]$ is the 2D center of all pixels around the intersection. With reference to the work of Tan et al. [13], the constants $a = 255$, $b = 1.5$, $c = 1.5$, and $\alpha = 0$ are selected for generating the ideal synthetic images.

The particle motion is simulated in a cubic volume of 40 × 40 × 40 mm^3, with the origin located at the origin O of the world coordinate system [40]. This framework represents the magnification of a small volume in the isotropic-turbulence flow from JHTDB. The image resolutions of all cameras are fixed at 2,000 × 2,000 pixels to capture all particles in the cubic volume with or without different refractive interfaces. To compare the performances of STB algorithms with different camera models under the same particle density with or without different refractive interfaces, the camera layout remains unchanged, but the image zone with particles varies as shown in Fig. 5, which provides detailed views of synthetic particle images with a resolution of 2,000 × 2,000 pixels for a $\text{ppp}_{\text{mean}} = 0.05$ (ppp denotes particles per pixel). Due to the deflection of the *LOS*, the image zone with particles from the plane interface of the octagonal tank (750 × 750 pixels) is larger than that (600 × 675 pixels) without any interfaces. To account for higher refractive distortion, each camera has a fixed resolution of 2,000 × 2,000 pixels. Moreover, in the cubic area of each condition, the particle image density varies between 0.01 and 0.07 ppp within different zones of the camera images, with an average particle image density of approximately 0.05 ppp. The motions of 400,000 particles are simulated according to an initial density of 0.10 ppp. Then, the projected particles under each refractive interface are randomly selected, with the number controlled by the particle image density according to the image zone size. The particle image density is set as 0.01, 0.025, 0.05, 0.075, and 0.10 ppp.

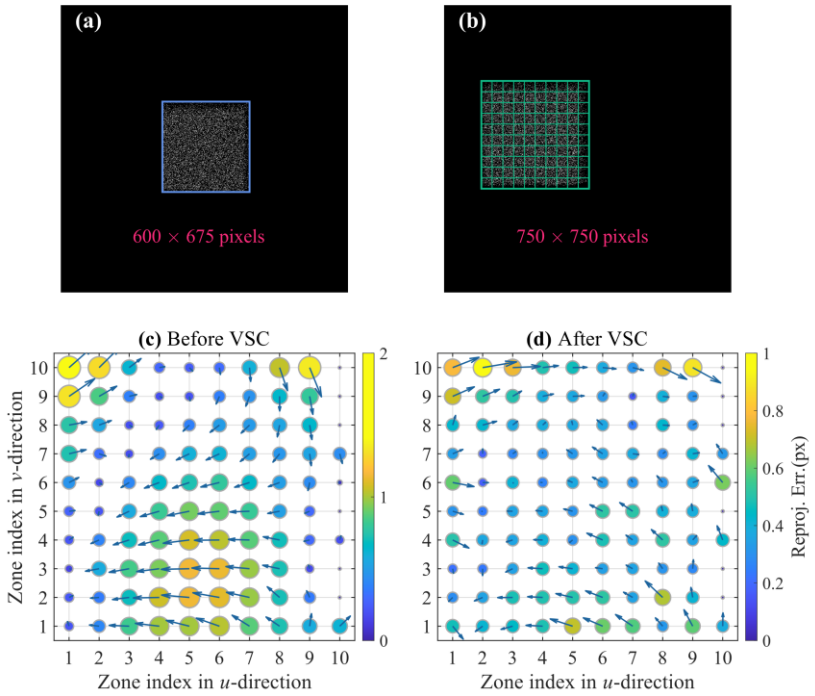

Figure 5 Detailed views of synthetic particle images with a resolution of 2,000 × 2,000 pixels in the image center of camera 1 for ppp_{mean} = 0.05. To record all the particles under a higher refractive distortion, each camera has a fixed resolution of 2,000 × 2,000 pixels. In the boxed area of each condition, the particle image density varies between 0.01 and 0.07 ppp within the camera images, and the particle image density averaged over the complete image is approximately 0.05 ppp. (a) Without refractive interface. (b) Planar wall of the octagonal water tank with a thickness of 20 mm. (c-d) Comparison of calibration errors in different regions of image before and after VSC.

After obtaining the synthetic calibration and particle images with the interface, the camera calibration for the pinhole camera model and the two-plane polynomials was performed with the synthetic calibration images. Then the VSC procedure [14] for the pinhole camera model was executed with the synthetic particle images with its particles corresponding 3D position. From the comparison of calibration errors in different regions of the image before and after VSC in Fig. 5c–d, the VSC cannot correct all the calibration deviation caused by the refractive interface, although it successfully reduces calibration errors in some regions, some errors are still over 1.5 px. The reason may be that the classical pinhole camera model with distortion parameters is too linear and cannot capture the nonlinearities for 3D space to the 2D image plane in the refractive imaging system. For the 3rd-order two-plane polynomials calibration, the mean reprojection errors of particles in cases with the refractive interface are all lower than 0.1 px from Fig. 2f without VSC. The reprojection errors are small by the two-plane polynomials calibration, which is a better selection for STB.

3.2 Computational accuracy and efficiency

Table 2 Configuration parameters for the performance comparison of OpenLPT and LOSC-LPT

Configuration parameters	OpenLPT	LOSC-LPT
Number of iterations	4(0)[1]	4(0)[1]
Number of shake iterations	6	6
2D intensity threshold	20[2]	20[2]
Initial shake width (px)	0.5	0.5
Allowed triangulation error (px)	0.6	0.6
Physical unit of image pixel (mm/px)	0.02	0.02
Search radius without predictor (px)	10	10
Search radius with predictor (px)	0.5	0.5
Particle intensity threshold	0.1 I_{avg}	0.1 I_{avg}
Projection factor	1	1
Predictor for initialization	Particle–space correlation	Particle–space correlation

Number of passes	1	1
Hardware	Intel® Xeon® Gold 6230	Intel® Xeon® Gold 6230
Number of cores	40 cores/80 threads, 2.1GHz	40 cores/80 threads, 2.1GHz
Runtime environment	gcc 8.1.0	gcc 8.1.0

Note: 1-The number in brackets indicates the number of iterations for a reduced camera, which is not applied in this work.
2-The maximum image intensity is 255.

The accuracy, convergence, and robustness of the LOSC-LPT framework are evaluated at a high image density of up to 0.10 ppp without any wall interfaces. The performance of the proposed framework is compared with OpenLPT, which uses the pinhole Tsai camera model [13] based on the STB [1] algorithm. Figure 6 presents the percentages of detected particles (F_d), ghost particles (F_g), and position uncertainty (Δp, reconstructed error) as functions of snapshot series. These three quantities serve as key indicators of the convergence performance of the framework under a high image density. Cases with image densities over 0.10 ppp are not considered, as such conditions (> 0.10 ppp) are typically not encountered in real experiments. The configuration parameters for the performance comparison of OpenLPT and LOSC-LPT are summarized in Table 2. The same conditions are used to ensure a fair comparison across different frameworks. The computation time required by the OpenLPT and LOSC-LPT frameworks is determined using a multi-core CPU (Intel® Xeon® Gold 6230) in the high-performance computing supercomputing cluster located at Shanghai Jiao Tong University.

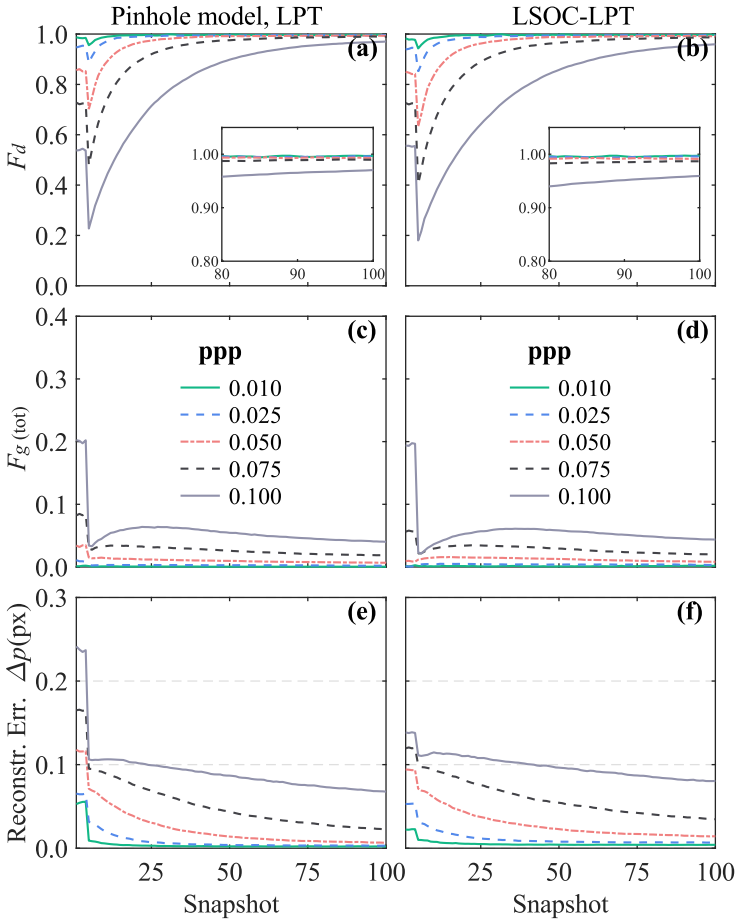

Figure 6 (a)(b) Total number of detected particles relative to the number of true particles by OpenLPT and LOSC-LPT in a scenario without any wall interfaces. (c)(d) Total number of reconstructed ghost particles (tracked and untracked) relative to the number of true particles. (e)(f) 3D positional error in a pixel, averaged over all tracked particles relative to the true particle position.

Figure 6a shows that in the absence of a refractive interface, LOSC-LPT and OpenLPT exhibit similar convergence in terms of the total number of detected particles relative to the number of true particles (F_d) for all image densities. For example, using IPR, the mean F_d of the particle cloud in the first four frames at 0.05 ppp is 84.51% by LOSC-LPT, slightly lower than that of

OpenLPT (85.56%). The F_d of the particle cloud exhibits complete convergence when the snapshot series reaches 100 frames, with the values being 99.11% for LOSC-LPT and 99.28% for OpenLPT. At a density of 0.10 ppp, the percentage of detected particles by LOSC-LPT is slightly lower than that by OpenLPT in each snapshot, which means that the complete convergence time for LOSC-LPT is longer. This difference is attributable to the reprojection algorithm during the shaking process based on LOS interpolation, because some reprojection errors of particles by LOS interpolation are over 0.1 px from Fig. 2f. Then the least square solution (some triangulation points) of the LOSs from all cameras is slightly different from the particle X, Y, and Z-position from Fig. 7a, which shows that some reconstructed particle positions deviate from the exact particle positions. To address this, the LOSC strategy is introduced to refine the 3D particle position, and the strategy can improve accuracy of particle positions effectively from Fig. 7b. During the process of shaking the 2D particle center, i. e. LOSC, in the image, the sum $I_{\text{res.}}$ of residual image pixels is locally optimized when multiple particles overlap at the same position in the image, which may cause a slightly slower convergence. Although LOSC leads to slightly slower convergence, an F_d of over 99.50% is reached when the snapshot reaches 120 at 0.05 ppp. For the percentage of ghost particles F_g, as shown in Fig. 6b and consistent with the findings of Tan et al. [13], OpenLPT outperforms STB (Schanz et al. [1] in reducing the number of ghost particles during IPR. Compared with the OpenLPT framework, LOSC-LPT has fewer ghost particles when the image density is less than 0.10 ppp, although the percentage is higher in the first four frames; this is attributable to the use of LOSC during track initialization. Local optimization during LOSC helps reduce the number of ghost particles because many overlapped particles are used only once. In addition, as shown in Figs. 6e-f, the 3D mean positional error in pixels (averaged over all tracked particles relative to the true particle position) by LOSC-LPT is slightly larger than that computed by OpenLPT (1e-6), likely because of the larger calibration error (1e-3 px), and the mean 3D positional error remains acceptable at approximately 0.054 px (2.7e-3 mm) for 0.10 ppp. Note that if LOSC is not applied, the mean reconstruction errors of all 3D particles are much larger as shown in Fig. 7c, and after LOSC the errors can be reduced to less than 0.1 px in Fig. 7d, which indicates that the LOSC is necessary for STB using two-plane polynomials. Overall, the comparative discussion without refractive interfaces indicates that the LOSC-LPT framework exhibits similar accuracy and convergence performances as OpenLPT.

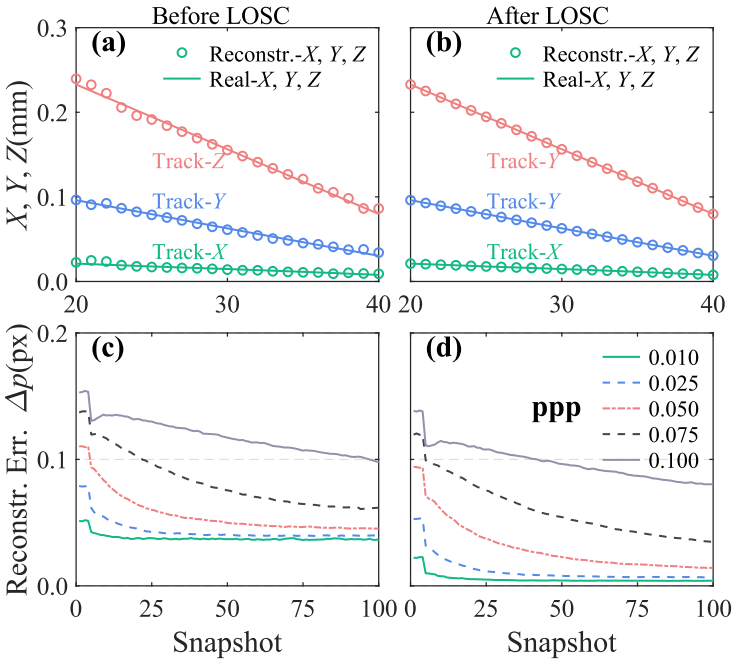

Figure 7 (a) The comparison of the x, y, and z component positions of the reconstructed track with the positions of real particles before LOSC. (b) The comparison of the x, y, and z component positions of the reconstructed track after LOSC. (a) and (b) are obtained under 0.010ppp. (c–d) 3D positional error in pixels, averaged over all tracked particles relative to the true particle position, (c) represents the statistical results before LOSC, (d) represents the statistical results before LOSC.

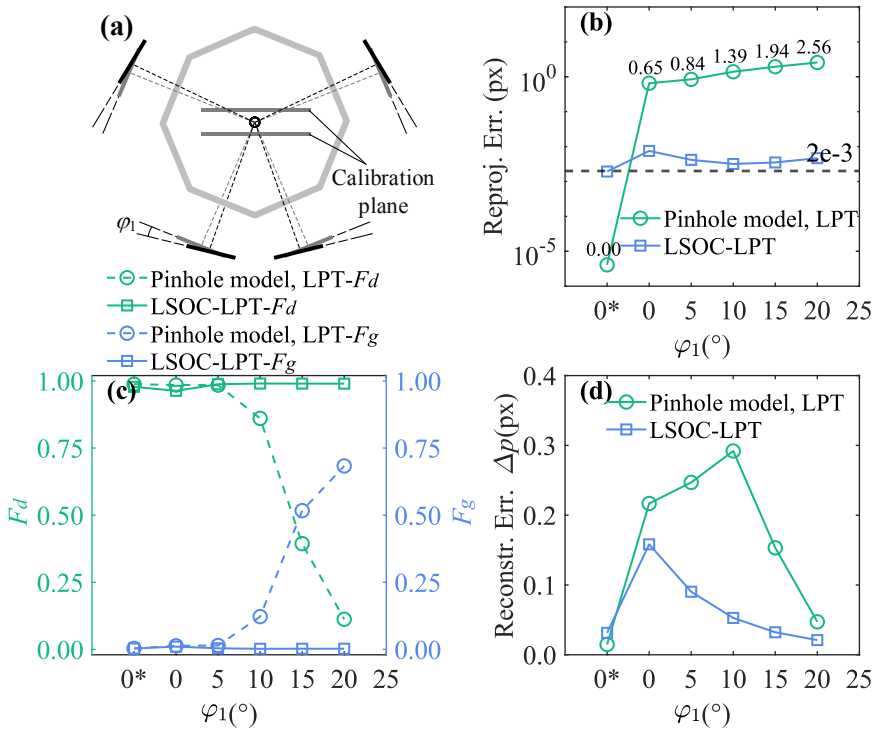

Figure 8 Comparison of reconstruction performance in different water tanks with refractive interfaces; ppp_{mean} = 0.05. (a) Cameras are not parallel to the wall of the octagonal tank. (b) Maximal reprojection error. (c) Comparison of numbers of ghost or detected particles relative to the number of true particles, F_g and F_d, respectively. (d) Mean reprojection error of detected particles.

When the cameras are not parallel to the wall of the octagonal tank (Fig. 8a), an angle φ_1 exists between the camera optical axis and normal to the wall. Compared with the condition without refractive interfaces, Figure 8b shows the maximal calibration error by the pinhole Tsai camera model suddenly increases to 1.0 pixel even when φ_1 is 0°, and it continues to increase linearly with the angle φ_1. In contrast, the maximal reprojection error by the polynomial mapping function remains constant at 2e-3 px. As shown in Fig. 8c, when the pinhole Tsai camera model is used, the percentage of detected particles (F_d) dramatically decreases as φ_1 increase, and more ghost particles are reconstructed. Furthermore, the position uncertainty increases as φ_1 decreases but decreases when φ_1 exceeds 5° (Fig. 8d) because the number of detected particles is smaller than that shown in Fig. 8d. In contrast, when the polynomial mapping function is used, the percentage of detected particles does not change because the reprojection error is maintained at 2e-3 px, resulting in a small number of ghost particles.

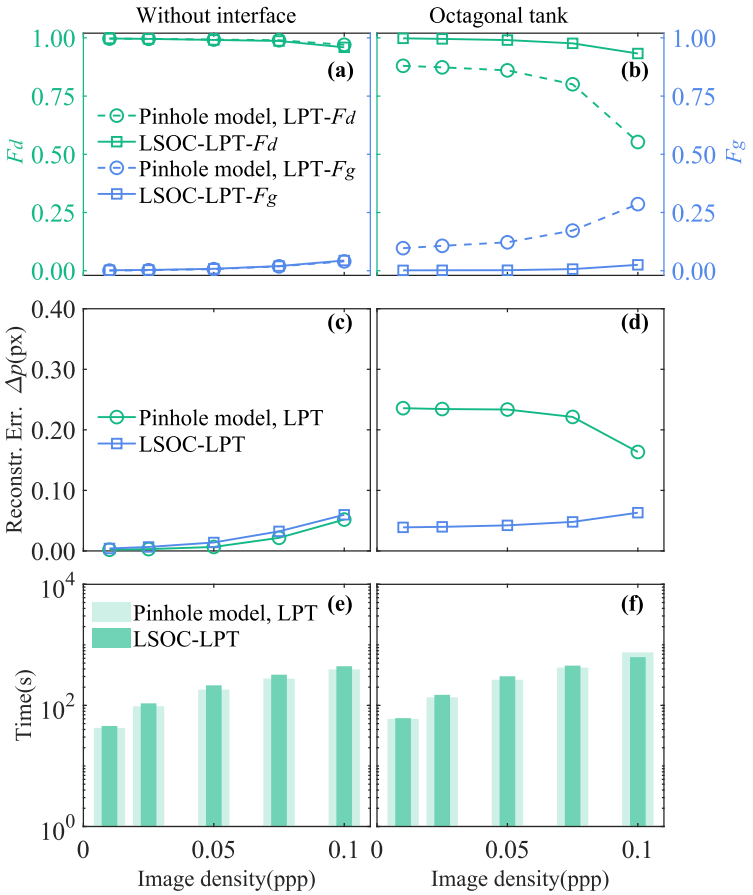

Figure 9 Comparison of reconstruction performance in different water tanks with increasing particle concentration. All cameras are rotated by 10° around the X axis of the fixed world coordinate system, $\varphi_1 = 10°$. (a–b) Comparison of the numbers of ghost or detected particles relative to the number of true particles, F_g and F_d, respectively. (c–d) Mean errors of detected particles. (e–f) Mean IPR time per frame.

Figure 9 presents a comparison of the reconstruction accuracy, robustness, and efficiency in different water tanks at image densities of 0.10, 0.025, 0.05, 0.075, and 0.10 ppp. When the refractive interface exists, all cameras are rotated 10° around the X axis of the fixed world coordinate system, $\varphi_1 = 10°$. In the absence of interfaces, the performances of OpenLPT with the Tsai camera model and LOSC-LPT framework with polynomial functions are similar under high image densities, and the calculation time is the same, as shown in Fig. 9a. When the refractive interface cannot be neglected, LOSC-LPT outperforms OpenLPT in terms of a higher percentage of detected particles (F_d), reduced number of ghost particles, and higher 3D reconstruction accuracy, as shown in Figs. 9b and d. The computational time for LOSC-LPT is slightly larger than that for OpenLPT due to the incorporation of LOSC. Figures 9c–d indicate that the position uncertainty (Δp) under different image densities by OpenLPT is greater than that by LOSC-LPT, and the computational times of the two frameworks are nearly identical from Figures 9e–f. The mean IPR time per frame is slower than STB by Schanz et al. [1], that may be caused by the different 2D particle identification method, the velocity field calculations (particle-space correlation), or optimization of particles position with the residual image during shaking, as well as the computer performance.

3.3 Three-dimensional flow-field reconstruction

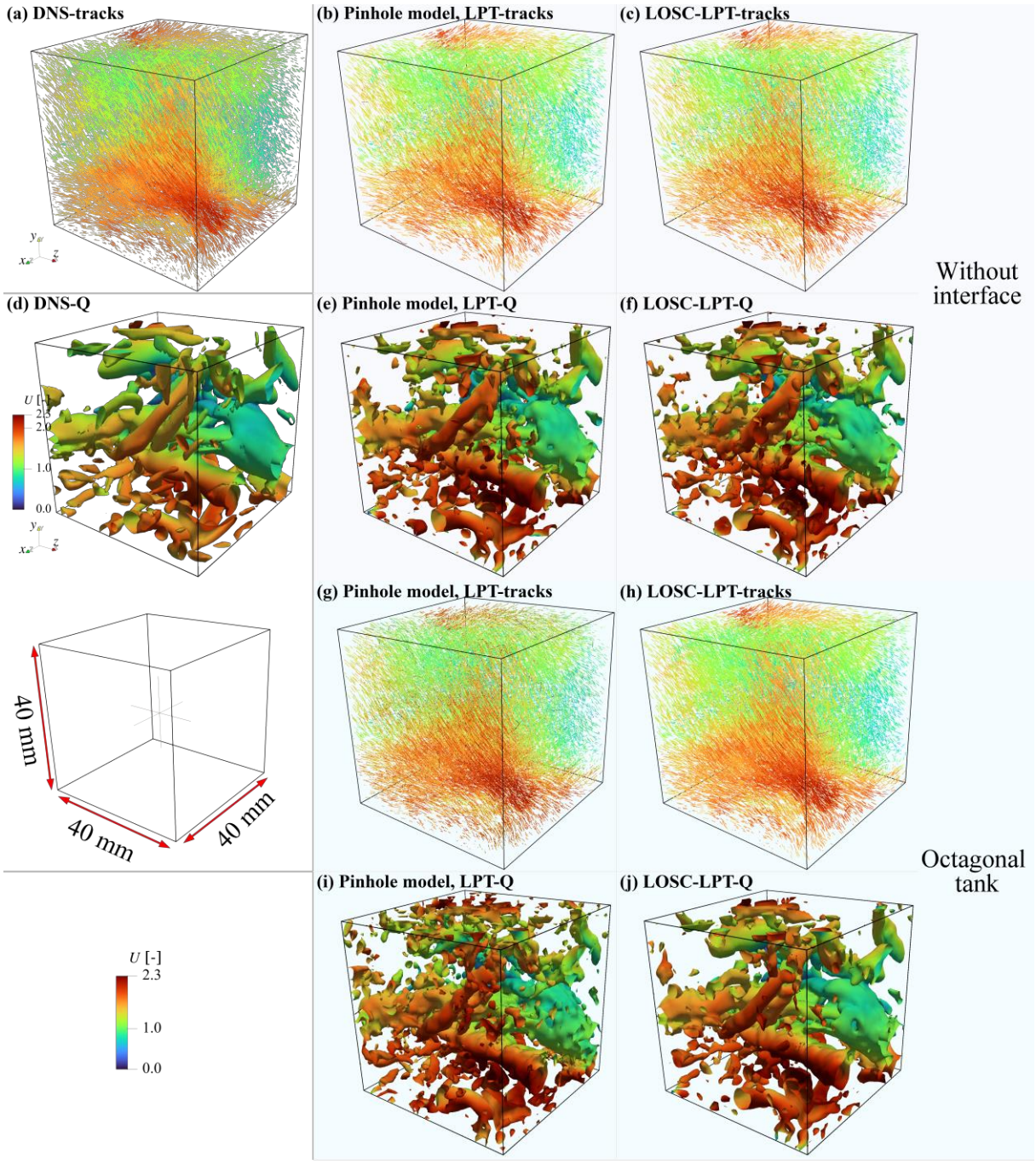

Figure 10 (a) 3D trajectories from DNS. (d) 3D flow field with Q = 120 [-] from DNS. (b, c, e, f) Results obtained using OpenLPT or LOSC-LPT without interfaces. (g-j) Results obtained using OpenLPT or LOSC-LPT in the octagonal water tank with φ_1 = 10°. Tracks represent the particle fields of the 105th–196th frames. Q is defined by the Q criterion.

The particle position errors along the tracks can be effectively eliminated using the track fitting procedure named TrackFit proposed by Gesemann [41], which approximates the optimal Wiener filter for our particle motion model. The cut-off frequency for assessing the contribution of the increment in particle acceleration to the cost function of all tracks is determined following the work of Gesemann [41]. To account for the large reconstruction errors near the track edges [42], a few points on each side of the track are removed from the final results. In this study, four points are removed on each side of the tracks in this work. The first 100 frames of the convergence phase are subtracted from the entire long track, based on Fig. 6. Using a synthetic image dataset of 200 frames with an image density of 0.05 ppp, the reconstructed 3D trajectories by OpenLPT and by LOSC-LPT are shown in Fig. 10. The first 100 frames of the tracks and four points on each side of the tracks are removed, and the

cases involve an octagonal water tank with φ_1 = 10°. The tracks correspond to the 105th–196th frame-based particle cloud. Compared with the DNS-Tracks in Fig. 10a from JHTDB [30], when the refractive interfaces do not exist, both OpenLPT and LOSC-LPT framework exhibit a high accuracy. The number of tracks in Fig. 10a is approximately 21,000 at a density of 0.05 ppp in an area of 600 × 675 pixels (Fig. 6a). The percentages of exactly reconstructed 3D trajectories for both OpenLPT and LOSC-LPT are more than 99% without the refractive interface. Several incorrect tracks are also observed in Figs. 10b–c, which may have been caused by overlapping particles at a high image density of 0.05 ppp. When refractive interfaces are present, the performance of OpenLPT using the Tsai camera model deteriorates, as shown in Fig. 10g, and most of the tracks contain high levels of noise due to the high reprojection error (Fig. 8b). In contrast, LOSC-LPT produces tracks with low noise levels, as shown in Fig. 10h, owing to the small reprojection error obtained using polynomial mapping functions (Fig. 8b).

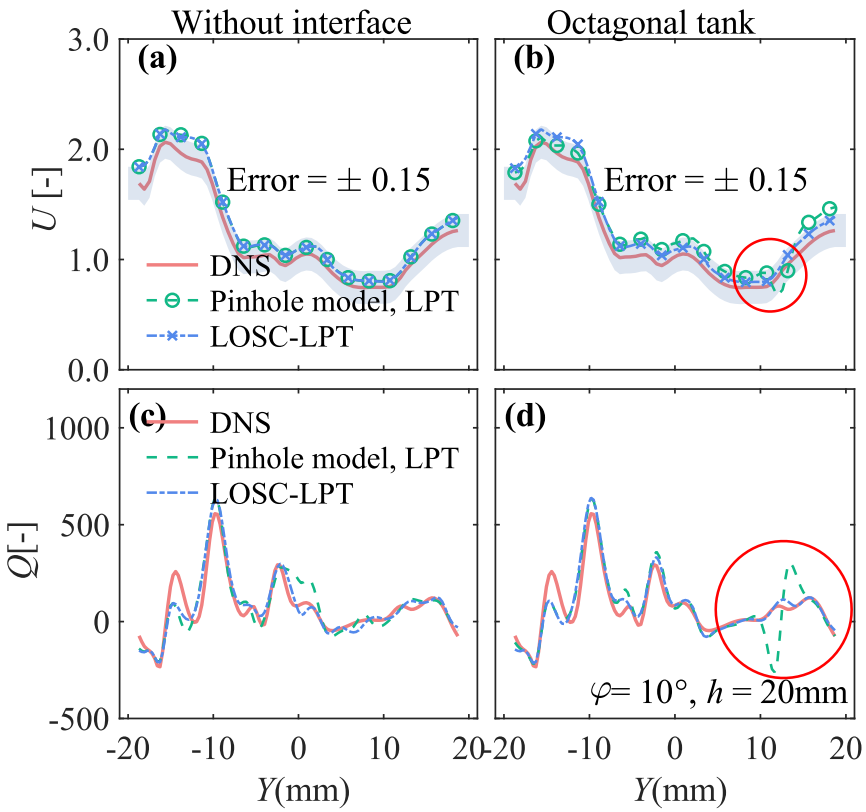

Figure 11 Comparison of flow field along the *y*-axis in different water tanks: (a-b) Velocity components. (c-d) *Q* criteria in the flow fields.

Additionally, the velocity and acceleration are extracted as the first and second derivatives of each track using the TrackFit method [41]. The flow field containing velocity and pressure can be interpolated into the Eulerian grid with the velocity and acceleration of discrete particles through adaptive Gaussian windowing [43], FlowFit [44], or vortex-in-cell plus [45]. In this study, the FlowFit method by Gesemann et al. [44] is used for the Eulerian flow-field interpolation, and this work realized the *div*1 version of FlowFit with only the penalization of divergence (for a velocity field of an incompressible flow) is performed and the divergence can also be represented as a linear combination of the unknown coefficients at any point in this volume. Figure 10 presents the comparison of different flow fields with the DNS flow field, with or without an interface (with the iso-surface of vorticity Q = 120 [-]). The vorticity results with the Q criterion shown in Figs. 10d–f indicate that with the accurate tracks, the flow field can be precisely recovered, and almost all vortex structures can be reconstructed. However, in the octagonal water tank with φ_1 = 10°, the flow field reconstructed by OpenLPT and LOSC-LPT are considerably different, with the flow field by OpenLPT exhibiting higher levels of noise. The reconstruction by LOSC-LPT is more accurate than the DNS-Q distribution (Fig. 10d). Figure 11 compares the flow field velocity magnitude U and Q criteria along the *y*-axis. In the octagonal water tank (Figs. 11b–d), in several local regions, the error generated by OpenLPT using the pinhole camera model is considerably larger than that generated by LOSC-LPT. A significant deviation exists between the pinhole-model solution and the DNS or LOSC-LPT solution may be caused by some strongly deviating tracks, which can be removed by a-posteriori outlier filtering based on neighboring tracks. The velocity error induced by LOSC-LPT using the polynomial camera model is

smaller than that of OpenLPT because the number of strongly deviating tracks is small, which highlights its superior robustness and stability.

Overall, the comparative analysis of the computational performances of the LOSC-LPT framework using polynomial functions and OpenLPT using the Tsai camera model indicates that the LOSC-LPT framework has a higher percentage of detected particles (F_d), fewer ghost particles (F_g), and smaller position uncertainty (Δp). Moreover, it can accurately reconstruct the flow field even when refractive interfaces are considered. This framework is thus applied for the experimental measurement of a jet from an elliptical nozzle involving refractive interfaces, as discussed in Section 4.

4. Application to elliptical jet flow

4.1 Experimental setup

The LOSC-LPT framework is experimentally validated in an octagonal tank (with each side measuring 250 mm and a height of 900 mm) filled with tap water [46], as shown in Fig. 12a. The vertical octagonal tank is designed to study the fluid dynamics of 3D jet flow at a high Reynolds number (Re). The nozzle outlets are deformable, and thus jet experiments with different geometrical shapes can be conducted in this octagonal tank. An elliptical nozzle with an aspect ratio $AR = 2$ (defined as the ratio of the semi-major axis length a to the semi-minor axis length b of the elliptical nozzle) is installed at the bottom of the octagonal tank. The equivalent diameter is $D_e = 20$ mm, calculated based on the diameter of a circular jet with a momentum flux equal to that of the elliptical jet with exit semi-major and semi-minor axes a and b respectively, i.e., $D_e \equiv 2(ab)^{1/2}$ [47]. Re is set as 3,000 according to the equivalent diameter and inlet velocity. The geometrical shape of the elliptical nozzle is designed with a contraction ratio of 5:1 from a circular cross-section (diameter $D_i = 100$ mm) to an elliptical cross-section. The contraction length is approximately $1.6D_i$ and the contraction profile of the elliptical nozzles follows a third-order polynomial curve with short straight portions at both upstream and downstream ends [48].

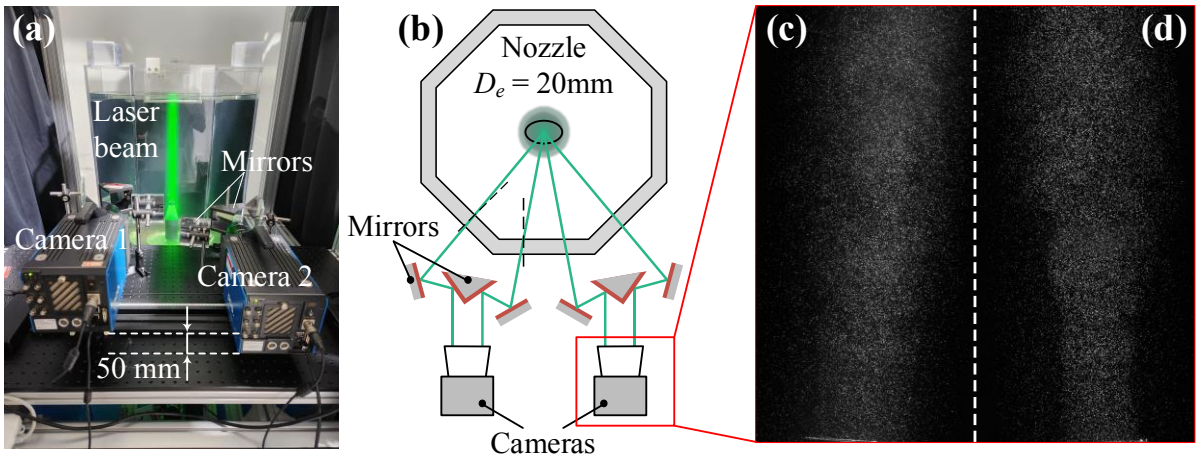

Figure 12 (a) Experimental setup and camera configuration. (b) Top view of two cameras with mirrors and their relative positions. (c)(d) Two views obtained from camera 2 by cropping the particle image.

For flow visualization, 50-μm polyamide tracer particles (Dantec, Denmark) are seeded into the octagonal tank, and the nozzle is illuminated with a 25-W continuous-wave laser operating at 532 nm (Millennia EV25S, USA). The volumetric light is expanded and reflected through a flat-concave lens system to ensure that a 50 mm thick light beam illuminates the jet longitudinal plane. Particle images are recorded in continuous acquisition mode using two 12-bit complementary metal-oxide-semiconductor cameras (PCO, Germany) and a lens of 100 mm with a spatial resolution of 2,000 × 2,000 pixels. The cameras achieve a continuous sampling rate of 2,000 image pairs per second, the total sampling time is 3 s, and 6,000 image sets are recorded. The particle size in each image is approximately 3 × 3 pixels, and the particle density is approximately 0.02 ppp. Using mirrors, as indicated by the green dashed line for the top view of the two cameras and their relative positions in Fig. 12b [49], four different views with image resolutions of 1,000 × 2,000 pixels in the radial direction can be obtained using only two cameras. Further details of the experimental setup can be found in the literature [50].

For the LOSC-LPT framework, the 3D volumetric calibration of each camera is realized using a checkerboard plane with a grid size of 5 mm, and a 30-mm normal shift (-15 ~ 15 mm, step size is 2mm) of the calibration plate is achieved through a traversal mechanism. The precision of the traversal mechanism is 0.02 mm, which corresponds to 0.1 pixel in the image (Fig. 12c). All the particles are reconstructed in a volume with dimensions of 50 mm ($2.5D_e$ in the x-direction) × 100 mm ($5D_e$ in the y-direction) × 50 mm ($2.5D_e$ in the z-direction). The mapping functions from the 3D space to the 2D image for each camera are calibrated using the Tsai camera model for the OpenLPT framework and the two-plane polynomial camera model for the proposed LOSC-LPT framework.

4.2 Experimental results and discussion

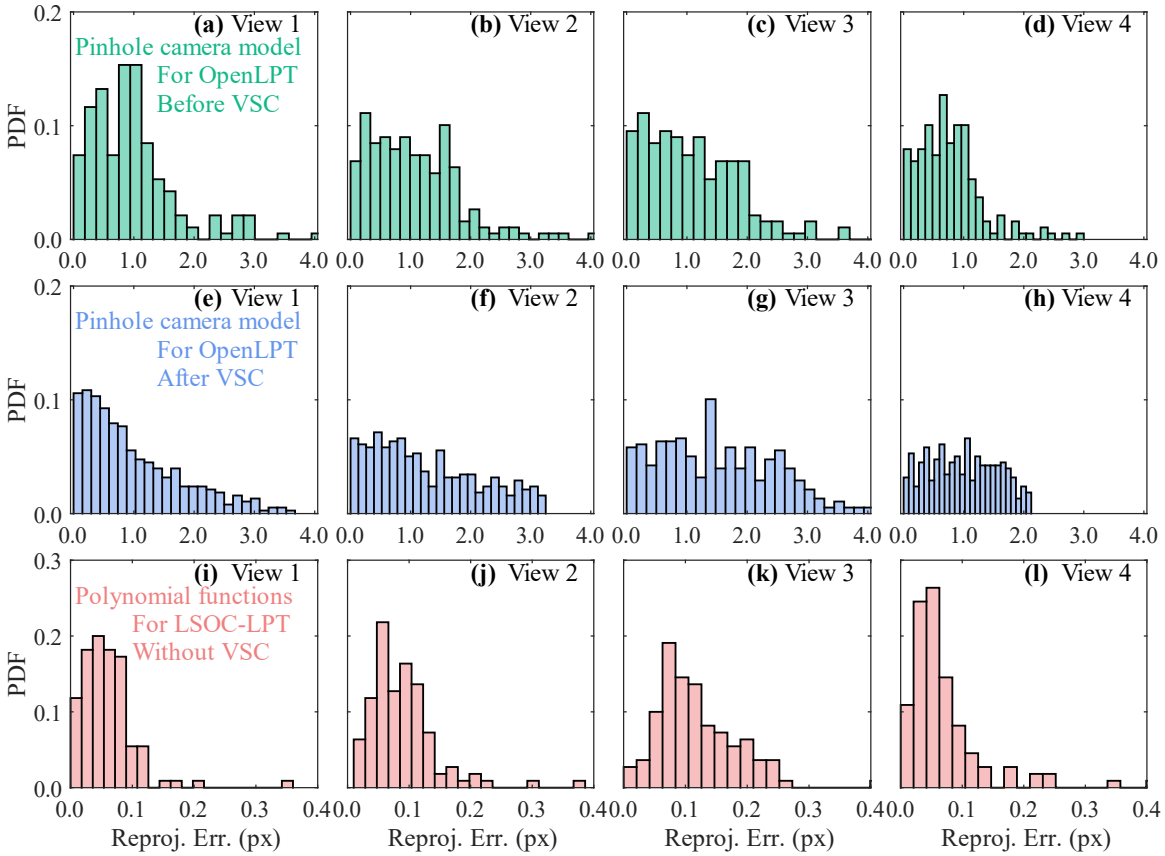

Figure 13 Comparison of calibration errors from the application of the different camera models in the elliptical jet experiment, (a-d) Pinhole Tsai model before VSC, (e-h) Pinhole Tsai model after VSC, (i-l) Calibration based on two planes using a third-order polynomial.

Owing to the use of mirrors, as shown in the top view of the two cameras and their relative positions in Fig. 12b, only two cameras are required [49] to obtain four different views in the radial direction, which helps reduce the hardware cost of 3D measurement using Tomo-PIV or 3D LPT. While determining the angle between the camera optical axis and normal line of the window is challenging. Moreover, the refractive interfaces prepared using acrylic material cannot be neglected, resulting in significant calibration uncertainty. Figure 13 compares the calibration errors associated with the calibration based on the pinhole Tsai camera model using a third-order polynomial in the elliptical jet experiment, two planes at -15 mm and +15 mm are used. The maximal calibration errors using the pinhole Tsai model in four views are larger than 3.0 px (Figs. 13a–d), and the mean calibration errors are approximately 1.0 px. Although the VSC has been applied for improving the calibration accuracy by pinhole Tsai model, the mean calibration errors stay nearly 1.0 px from Figs. 13e–h. These values do not satisfy the high precision requirements of 3D measurement by LPT, because the calibration errors for Tomo-PIV or 3D LPT must be lower than 0.4 px [3] and preferably less than 0.1 px [14]. In contrast, when the polynomial mapping functions are used, as shown in Figs. 13i–l, the maximal calibration errors are less than 0.4 px, and the mean calibration errors are all less than 0.1 px. What's

more, then calibration plate from the range of -13 ~ + 13 mm (step size = 2 mm) can be used for the accuracy evaluation of static reprojection by LOS interpolation and triangulation reconstruction. The maximal reprojection errors using the pinhole Tsai model are larger than 3.0 px, and the mean calibration errors are over 1.0 px. These values do not satisfy the high precision requirements of 3D measurement by LPT which must be lower than 0.4 px. In contrast, when the polynomial mapping functions are used, the mean reprojection errors are over 0.5 px by Z-interpolation, while the mean reprojection errors are all less than 0.12 px by LOS interpolation. These findings demonstrate that polynomials can yield high-precision calibration parameters for 3D measurement techniques compared with the pinhole Tsai camera model.

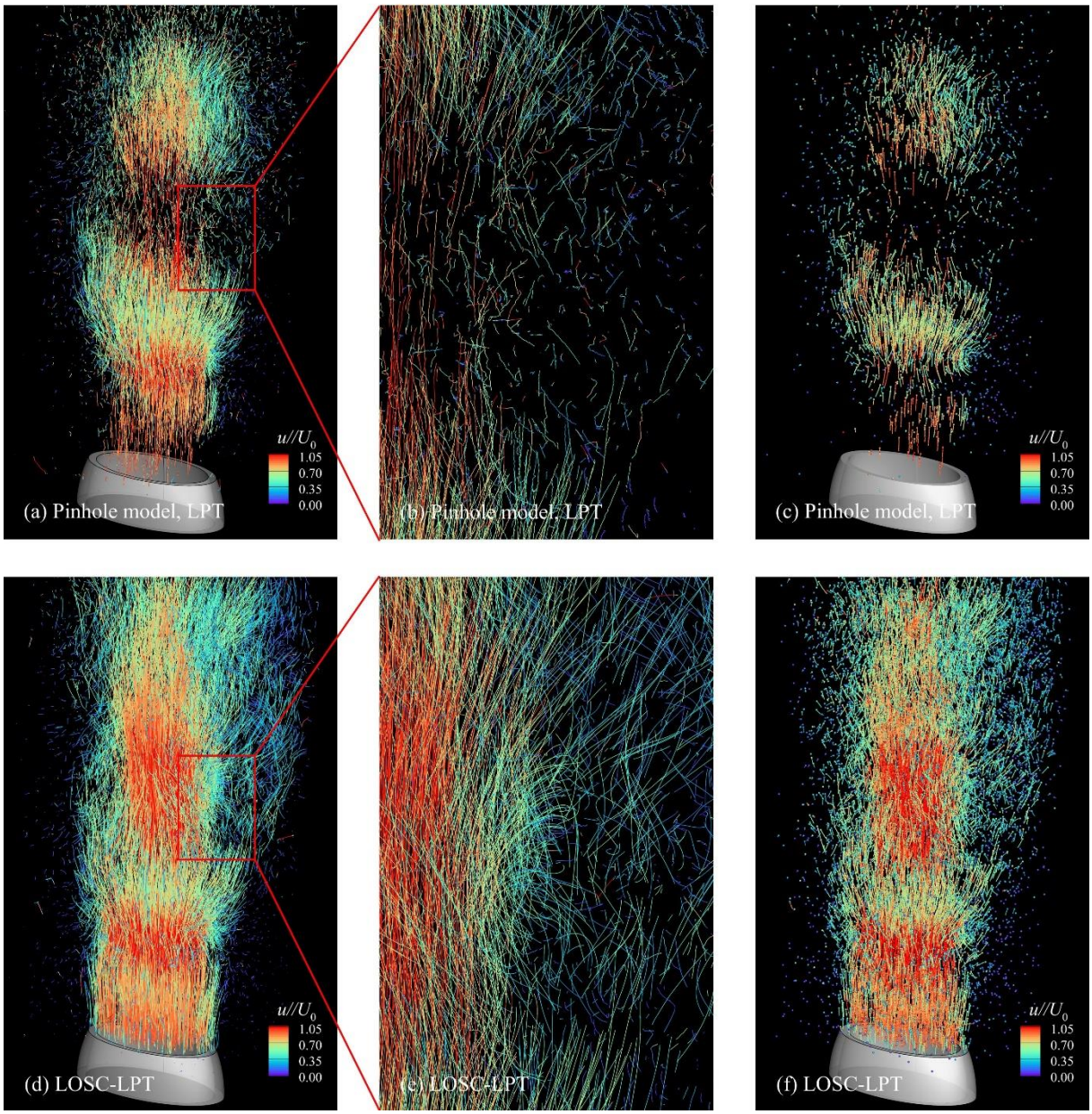

Figure 14 Sample particle trajectories from an elliptical jet, reconstructed by OpenLPT or LOSC-LPT. Overlay of 200 time-steps, colored by streamwise velocity via (a) OpenLPT or (d) LOSC-LPT. Trajectory details obtained using (b) OpenLPT or (e) LOSC-LPT. Tracked particles for single time-step (t_n, indicated by dots) with a tail of 50 time-steps (reaching back to t_{n-49}) by (c) OpenLPT or (f) LOSC-LPT.

For the elliptical jet with $AR = 2$, all current tracks are subjected to the TrackFit function after subtracting the first 100 frames of the tracks and removing four points on each side of the tracks [41]. Figure 14 presents the results from the track reconstruction based on OpenLPT and LOSC-LPT, showing the tracks of 100 successive time-steps out of 500 snapshots, colored by

streamwise velocity. The numbers of tracks obtained using OpenLPT and LOSC-LPT framework are considerably different (Fig. 14). The number of long trajectories generated by OpenLPT is no more than 4,500, whereas the LOSC-LPT generates more than 13,000 tracks. Figures 14b and 14e show the details of parts of all tracks by OpenLPT and LOSC-LPT, respectively. Although TrackFit is applied to fit all trajectories, the tracks generated by OpenLPT exhibit significant uncertainty. The tracked particles for a single time-step (t_n, marked by dots) with a tail of 50 time-steps (reaching back to t_{n-49}) by OpenLPT (Fig. 14c) and LOSC-LPT (Fig. 14f) are visualized to examine the trajectories near the passing elliptical vortex rings produced in the initial shear layer due to Kelvin–Helmholtz instability [47].

Subsequently, the interpolation of the Eulerian flow-field interpolation into 36 × 36 × 70 vectors is performed using the velocity and acceleration data of discrete particles obtained by the FlowFit method developed by Gesemann et al. [44]. Figure 15 shows the Eulerian flow field with iso-surfaces of $Q = 0.5\ U_0^2/D_e^2$ colored by streamwise velocity. For comparison, the Tomo-PIV result in Fig. 15a is reconstructed using a custom GPU-based Tomo-PIV framework [51]. Notably, the flow-field noise is large, and the non-zero divergence of velocity is significant (most absolute values greater than $0.11\ U_0^2/D_e^2$) in the Tomo-PIV data. Due to the inferior quantity and quality of tracks generated by OpenLPT (Fig. 14a), the instantaneous Eulerian flow-field interpolation based on tracks by OpenLPT is not ideal, and thus the flow field exhibits significant noise (Fig. 15b). The flow field interpolation based on the tracks generated by LOSC-LPT (Fig. 15c) is more accurate, which captures more complete coherent structures, such as the axial switching events of elliptical jet due to Biot–Savart self-induction [47, 52]. The axis-switching phenomenon in the elliptical jet signifies the evolution of the vortex ring structure, with expansion of the minor axis and rapid narrowing of the major axis. The major axis of the elliptical vortex ring switches in the downstream region of the jet exit. Figure 15c provides evidence of this axis switching as the major axis of the second elliptical vortex ring is different from that of the third elliptical vortex ring in the instantaneous flow field.

The application to the elliptical jet flow demonstrates that the LOSC-LPT framework using polynomial mapping functions has a smaller calibration error and higher accuracy for real 3D flow measurement with refractive interfaces than the OpenLPT framework using the pinhole Tsai camera model, resulting in the recovery of more complete vortical structures in the flow.

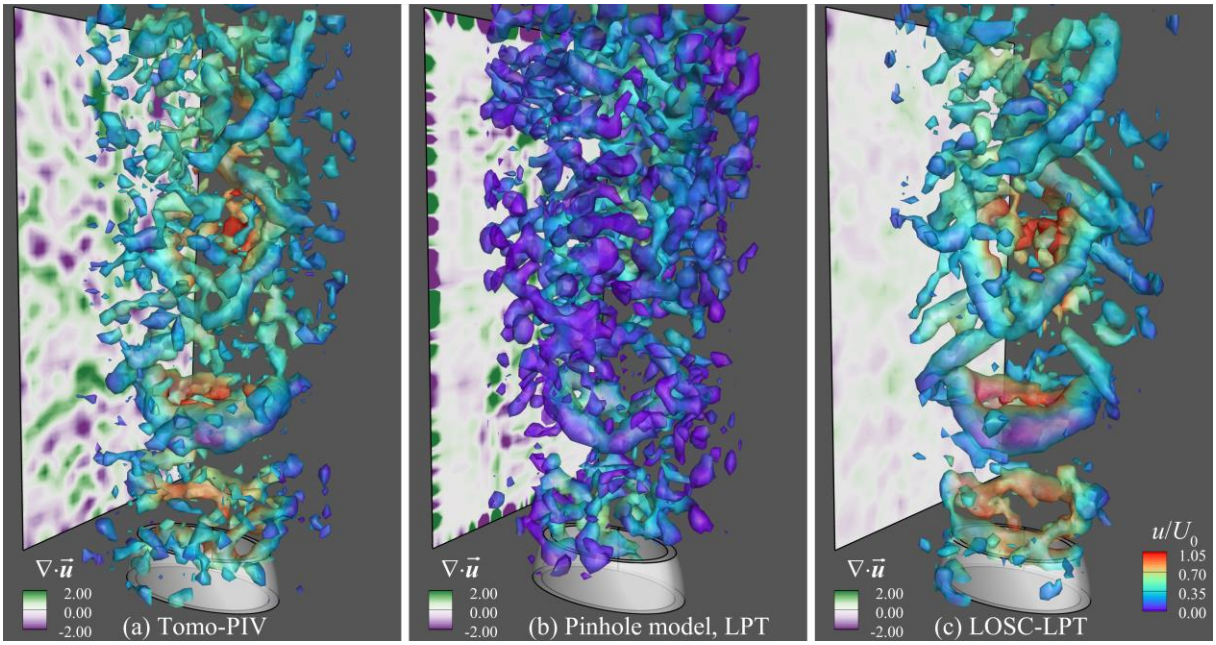

Figure 15 (a) Iso-surfaces of $Q = 0.5\ U_0^2/D_e^2$ colored by streamwise velocity, obtained by Tomo-PIV. (b) Eulerian flow field reconstructed by OpenLPT and FlowFit. (c) Eulerian flow field reconstructed by LOSC-LPT and FlowFit. All flow fields pertain to the same spatial resolution.

5. Conclusions

An improvement of the "Shake-The-Box (STB)" of LPT is provided using the polynomial calibration model in Tomo-PIV. The method (named LOSC-LPT) features innovative and effective strategies for incorporating polynomial mapping functions

in STB to realize particle stereo matching, 3D triangulation, IPR, and refinement of 3D particle position by shaking the LOS. This approach facilitates temporal domain particle tracking at high particle image densities, especially in scenarios commonly encountered in experimental fluid mechanics involving gas–solid–liquid interfaces at container walls. The proposed technique can enable accurate determination of the position, velocity, and acceleration of flow in LPT measurements, even in situations in which refractive interfaces cannot be neglected. The assessment of the LOSC-LPT framework using the synthetic image datasets and the experimental elliptical jet flow demonstrate the following conclusions:

(1) For noise-free images with a particle image density of up to 0.10 ppp without refractive interfaces, the accuracy, convergence, and robustness of the LOSC-LPT framework are identical with OpenLPT framework. For noise-free images at 0.05 ppp, more than 99.0% of the particles are detected (F_d); the percentage of ghost particles, F_g, is less than 0.04%; and the mean position uncertainty Δp is less than 0.015 px after convergence. Better results can be achieved at lower particle image densities.

(2) In scenarios with refractive interfaces, the maximal calibration error based on the Tsai camera model (> 1.0 pixel in synthetic image datasets) is larger than that induced by polynomial mapping functions (< 2e-3 pixel). When using OpenLPT based on the pinhole Tsai camera model, the number of detected particles can be retained, while the position uncertainty of the reconstructed particles increases to more than 0.2 px. When the angle φ_1 exists between the camera optical axis and normal to the wall is not equal to zero, based on the pinhole Tsai camera model, the number of detected particles decreases sharply to 5% ($\varphi_1 = 20°$). In contrast, the LOSC-LPT framework, which adopts polynomial mapping function calibration, can maintain high accuracy ($F_d > 99.00\%$), robustness ($F_g < 0.05$ %) and accuracy ($\Delta p < 0.15$ px). The 3D flow-field reconstructions by FlowFit demonstrate that the velocity error pertaining to LOSC-LPT is considerably smaller than that generated by OpenLPT.

(3) For the elliptical jet flow at Reynolds number Re = 3,000 in an octagonal tank with gas–solid–liquid interfaces, the maximal calibration errors using the pinhole Tsai model > 3.0 px, and the mean calibration errors ≈ 1.0 px. These values are considerably larger than those associated with the polynomial mapping functions (maximal calibration errors < 0.4 px and mean calibration errors < 0.1 px). The huge calibration errors by the pinhole Tsai model caused OpenLPT fails when the refractive interface exists.

(4) Owing to the large calibration errors, the number of long trajectories detected by OpenLPT is no more than 4,500, and excessive noise is introduced in the Eulerian flow-field interpolation. In contrast, the LOSC-LPT yields over 13,000 trajectories under small calibration errors. The LOSC-LPT recovers a more accurate 3D Eulerian flow field with a lower velocity divergence and captures axial switching events in the elliptical jet due to Biot–Savart self-induction.

The particle tracks and 3D flow-field reconstructions demonstrate that the LOSC-LPT framework can recover a more accurate 3D Eulerian flow field and capture more complete coherent structures in the flow, and thus holds great potential for widespread application in 3D experimental fluid measurements in scenarios with refractive interfaces.

Acknowledgements

Financial support from the National Natural Science Foundation of China (12272231 and 12227803) is gratefully acknowledged. The authors thank Prof. Yue YANG and Dr. Zhifeng LIU in Peking University for the generous provision of the 3D measurement data during the LOSC-LPT development and testing stage.

Ethics Declarations

This is submitted for publication consideration to *Measurement Science and Technology*. The manuscript has been neither published nor submitted elsewhere for publication. If accepted by *Measurement Science and Technology*, it will not be published elsewhere in the same form, in English or in any other language, without the written consent of the publisher.

Conflicts of Interest

The authors declare that they have no known competing financial interests or personal relationships that could have appeared to influence the work reported in this paper.

Data availability statement

The data that support the findings of this study are available upon reasonable request from the authors.

ORCID iDs

Xin Zeng https://orcid.org/0000-0002-9262-777X
Hao Qu https://orcid.org/0009-0005-3102-6849
Chuangxin He https://orcid.org/0000-0001-7953-9380
Yingzheng Liu https://orcid.org/0000-0002-1480-921X
Lian Gan https://orcid.org/0000-0002-4948-4523

References

[1] Schanz D, Gesemann S, Schrder A. Shake-The-Box: Lagrangian particle tracking at high particle image densities. *Experiments in Fluids*. 2016;**57**(5):70.
[2] Schröder A, Schanz D, Michaelis D, Cierpka C, Scharnowski S, Kähler CJ. Advances of PIV and 4D-PTV" Shake-The-Box" for turbulent flow analysis–the flow over periodic hills. *Flow, Turbulence and Combustion*. 2015;**95**(2):193-209.
[3] Elsinga GE, Scarano F, Wieneke B, Oudheusden BWV. Tomographic particle image velocimetry. *Experiments in Fluids*. 2006;**41**(6):933-47.
[4] Tsai RY. A versatile camera calibration technique for high-accuracy 3D machine vision metrology using off-the-shelf TV cameras and lenses. *IEEE Journal on Robotics & Automation*. 1987;**3**(4):323-44.
[5] Wieneke B. Iterative reconstruction of volumetric particle distribution. *Measurement Science and Technology*. 2013;**24**(2):827-37.
[6] Paolillo G, Astarita T. On the PIV/PTV uncertainty related to calibration of camera systems with refractive surfaces. *Measurement Science and Technology*. 2021;**32**(9).
[7] Elsinga GE. Tomographic particle image velocimetry and its application to turbulent boundary layers: Technische Universiteit Delft; 2008.
[8] Worth NA, Nickels TB, editors. A computational study of tomographic reconstruction accuracy and the effects of particle blocking. 5th Joint ASME/JSME Fluids Engineering Conference; 2007 2007.
[9] Ouellette NT, Xu H, Bodenschatz E. A quantitative study of three-dimensional Lagrangian particle tracking algorithms. *Experiments in Fluids*. 2006;**40**(2):301-13.
[10] Attanasi A, Cavagna A, Castello LD, Giardina I, Jelić A, Melillo S, Parisi L, Pellacini F, Shen E, Silvestri E, et al. GReTA-A novel global and recursive tracking algorithm in three dimensions. *IEEE Transactions on pattern analysis and machine intelligence*. 2015;**37**(12):2451-63.
[11] Kähler CJ, Astarita T, Vlachos PP, Sakakibara J, Hain R, Discetti S, La Foy R, Cierpka C. Main results of the 4th International PIV Challenge. *Experiments in Fluids*. 2016;**57**(6):97.
[12] Schröder A, Schanz D. 3D Lagrangian Particle Tracking in Fluid Mechanics. *Annual Review of Fluid Mechanics*. 2022;**55**.
[13] Tan S, Salibindla A, Masuk AUM, Ni R. Introducing OpenLPT: new method of removing ghost particles and high-concentration particle shadow tracking. *Experiments in Fluids*. 2020;**61**(2):1-16.
[14] Wieneke B. Volume self-calibration for 3D particle image velocimetry. *Experiments in Fluids*. 2008;**45**(4):549-56.
[15] Wieneke B. Improvements for volume self-calibration. *Measurement Science and Technology*. 2018;**29**(8).
[16] Jahn T, Schanz D, Schröder A. Advanced iterative particle reconstruction for Lagrangian particle tracking. *Experiments in Fluids*. 2021;**62**(8):179.
[17] Mulsow C. A flexible multi-media bundle approach. *International Archives of the Photogrammetry, Remote Sensing and Spatial Information Sciences - ISPRS Archives*. 2010;**38**:472-7.
[18] Belden J. Calibration of multi-camera systems with refractive interfaces. *Experiments in Fluids*. 2013;**54**(2):1-18.
[19] Westfeld P, Maas HG. 3-D least squares tracking in time-resolved tomographic reconstruction of dense flow marker fields. *Proceedings of the Commission V*. 2012.
[20] Feng M, Jia X, Wang J, Feng S, Zheng T. Global Calibration of Multi-Cameras Based on Refractive Projection and Ray Tracing. *Sensors (Basel)*. 2017;**17**(11).
[21] Liu W, Zhang Z, Gu Y, Zhai C. Fast and practical method for underwater stereo vision calibration based on ray-tracing. *Applied Optics*. 2023;**62**(17).
[22] Acher G, Thomas L, Tremblais B, David L. A new camera model combining an analytical model and a discrete correction to overcome refractive index variation challenges. *Measurement Science and Technology*. 2022;**33**(12).
[23] Paolillo G, Astarita T. Perspective Camera Model With Refraction Correction for Optical Velocimetry Measurements in Complex Geometries. *IEEE Trans Pattern Anal Mach Intell*. 2022;**44**(6):3185-96.
[24] Schanz D, Schröder A, Novara M, Geisler R, Agocs J, Kähler C. Large-scale volumetric characterization of a turbulent boundary layer flow. 13th International Symposium on Particle Image Velocimetry2019.
[25] Barta R, Bauer C, Wagner C, editors. pyPTV-a complete framework to reconstruct physical flow fields from camera images. 15th International Symposium on Particle Image Velocimetry; 2023; San Diego, California, USA.

[26] Soloff SM, Adrian RJ, Liu Z-C. Distortion compensation for generalized stereoscopic particle image velocimetry. *Measurement Science and Technology*. 1997;**8**(12):1441.
[27] Herzog S, Schiepel D, Guido I, Barta R, Wagner C. A Probabilistic Particle Tracking Framework for Guided and Brownian Motion Systems with High Particle Densities. *SN Computer Science*. 2021;**2**(6):485.
[28] Wei GQ, Ma SD, editors. Two plane camera calibration: a unified model. Proceedings. 1991 IEEE Computer Society Conference on Computer Vision and Pattern Recognition; 1991 3-6 June 1991.
[29] Deguchi K, Morishita I. A Unified Linear Camera Calibration Method Using Two Parallel Calibration Planes. *Transactions of the Society of Instrument and Control Engineers*. 1993;**29**(9):1023-32.
[30] Li Y, Perlman E, Wan M, Yang Y, Meneveau C, Burns R, Chen S, Szalay A, Eyink G. A public turbulence database cluster and applications to study Lagrangian evolution of velocity increments in turbulence. *Journal of Turbulence*. 2008;**9**(31):-.
[31] Tan S, Salibindla A, Masuk AUM, Ni R. An open-source Shake-the-Box method and its performance evaluation. 13th International Symposium on Particle Image Velocimetry; Munich, Germany2019.
[32] Zhang Z. A flexible new technique for camera calibration. *IEEE Transactions on pattern analysis and machine intelligence*. 2000;**22**(11):1330-4.
[33] Treibitz T, Schechner Y, Kunz C, Singh H. Flat Refractive Geometry. *IEEE Transactions on pattern analysis and machine intelligence*. 2012;**34**(1):51-65.
[34] Dracos T. Particle Tracking in Three-Dimensional Space. In: Dracos T, ed. *Three-Dimensional Velocity and Vorticity Measuring and Image Analysis Techniques: Lecture Notes from the Short Course held in Zürich, Switzerland, 3–6 September 1996*. Dordrecht: Springer Netherlands; 1996. p. 209-27.
[35] Mann J, Ott S. *Experimental Study of Relative, Turbulent Diffusion*. Risø National Laboratory1999.
[36] Clark A, Machicoane N, Aliseda A. A quantitative study of track initialization of the four-frame best estimate algorithm for three-dimensional Lagrangian particle tracking. *Measurement Science and Technology*. 2019;**30**(4).
[37] Novara M, Schanz D, Gesemann S, Lynch K, Schroeder A, editors. Lagrangian 3D particle tracking for multi-pulse systems: performance assessment and application of Shake-The-Box. 18th International Symposium on the Application of Laser and Imaging Techniques to Fluid Mechanics; 2016.
[38] Chandra R, Dagum L, Kohr D, Maydan D, Menon R. *Parallel Programming in OpenMP*: Parallel programming in OpenMP; 2001.
[39] Harish P, Narayanan PJ, editors. Accelerating large graph algorithms on the GPU using CUDA. 14th International Conference on High-Performance Computing; 2007 2007; Goa, India: Springer, Berlin, Heidelberg.
[40] Perlman E, Burns R, Li Y, Meneveau C, editors. Data exploration of turbulence simulations using a database cluster. Proceedings of the ACM/IEEE Conference on High Performance Networking and Computing; 2007 2007, November 10-16, 2007, Reno, ; Nevada, USA, SC
[41] Gesemann S. From particle tracks to velocity and acceleration fields using B-splines and penalties. *arXiv preprint arXiv:1510.09034*. 2015.
[42] Bobrov M, Hrebtov M, Ivashchenko V, Mullyadzhanov R, Seredkin A, Tokarev M, Zaripov D, Dulin V, Markovich D. Pressure evaluation from Lagrangian particle tracking data using a grid-free least-squares method. *Measurement Science and Technology*. 2021;**32**(8):084014.
[43] Agüí JC, Jimenez J. On the performance of particle tracking. *Journal of Fluid Mechanics*. 1987;**185**:447-68.
[44] Gesemann S, Huhn F, Schanz D, Schröder A, editors. From noisy particle tracks to velocity, acceleration and pressure fields using B-splines and penalties. 18th International Symposium on the Application of Laser and Imaging Techniques to Fluid Mechanics; 2016 2016.
[45] Schneiders JFG, Scarano F. Dense velocity reconstruction from tomographic PTV with material derivatives. *Experiments in Fluids*. 2016;**57**(9):1-22.
[46] He C, Liu Y, Gan L. Dynamics of the jet flow issued from a lobed Nozzle: Tomographic particle image velocimetry measurements. *International Journal of Heat and Fluid Flow*. 2021;**89**:108795.
[47] Hussain F, Husain HS. Elliptic jets. Part 1. Characteristics of unexcited and excited jets. *Journal of Fluid Mechanics*. 1989;**208**:257-320.
[48] Zeng X, Zhang Y, He C, Liu Y. Dynamics and entrainment mechanism of the jet flows from an elliptical nozzle: time-resolved tomographic PIV measurements. *Experiments in Fluids*. 2023;**64**(8).
[49] Bardet PM, Peterson PF, Savaş Ö. Split-screen single-camera stereoscopic PIV application to a turbulent confined swirling layer with free surface. *Experiments in Fluids*. 2010;**49**(2):513-24.
[50] Zeng X, Zhang Y, He C, Liu Y. Time-and frequency-domain spectral proper orthogonal decomposition of a swirling jet by tomographic particle image velocimetry. *Experiments in Fluids*. 2023;**64**(1):1-27.
[51] Zeng X, He C, Liu Y. GPU-accelerated MART and concurrent cross-correlation for tomographic PIV. *Experiments in Fluids*. 2022;**63**(5):1-18.
[52] Mitchell DM, Honnery DR, Soria J. Near-field structure of underexpanded elliptic jets. *Experiments in Fluids*. 2013;**54**(7):1-13.